UNIVERSITY OF COPENHAGEN

MSc in Physics

Flavour Identification Techniques

Development of algorithms for tagging of b- and c- quark for precise measurement of branching fractions of Higgs boson produced in electron-positron collisions

Kunal Gautam

Supervised by Mogens Dam

August 2020

Kunal Gautam
Flavour Identification Techniques
MSc in Physics, August 2020
Supervisors: Mogens Dam

University of Copenhagen
Faculty of Science
Niels Bohr Institute
Blegdamsvej 17
2100 Copenhagen Ø

"*The important thing is not to stop questioning. Curiosity has its own reason for existence. One cannot help but be in awe when he contemplates the mysteries of eternity, of life, of the marvelous structure of reality. It is enough if one tries merely to comprehend a little of this mystery each day.*"

Albert Einstein, 1955

"*Forty-two.*"

Douglas Adams, The Hitchhiker's Guide to the Galaxy

Preface

This thesis presents the study conducted as a part of my Master of Science degree in Physics at the Niels Bohr Institute of the University of Copenhagen. It aims to present a few techniques that can be used for the identification of hadronic decay events at an electron-positron collider. These techniques have been studied for simulated collission events in an environment compatible with the IDEA detector concept, which is being developed for FCC-ee. The theoretical analysis of the relevant underlying mechanisms and the technical introduction of the experimental set-up has been presented in a clear and instructive way, and I have tried to justify the suggested methods to the best of my abilities.

Acknowledgements

Foremost, I would like to express my deepest gratitude to my supervisor, Mogens Dam, who has been an exceptional mentor and a friend. He guided and encouraged me at every step of this project, no matter how hard things got. He inspired me to never stop asking questions and provided me with a learning environment beyond what I had ever expected. And even when the unprecedented situation arrived, with every institution being shut down due to Covid-19, he has been a persistent help.

I want to show my appreciation to Franco Bedeschi, whose assistance has been crucial for this project. I wish to thank my friends for all the spirited discussions we have had and for being there for constant support. I would like to particularly acknowledge the help and the invaluable assistance provided by Trina Naskar.

Let me take this opportunity to recognise the support of my parents, Jagdish and Krishna Gautam, and my brother, Tushar Gautam, who have been an endless source of motivation and love, and have always encouraged me to pursue my love for physics.

Abstract

Over time several algorithms have been developed for flavour identification/tagging for various colliders. There is an advantage in studying a newly discovered particle in electron-positron colliders since they allow to study this particle in a clean environment, owing to the fact that the incoming particles do not leave any residuals, unlike the QCD background in hadron collisions. In hadron colliders, in addition, the initial state is not known precisely, which further limits the high-precision measurements. This thesis reports on the study and implementation of flavour identification algorithms to distinguish the hadronic decay channels of the Higgs boson. The study has been performed in an environment compatible with proposed future e^+e^- circular colliders like the Future Circular Collider (FCC).

The first algorithms presented here is the Impact Parameter Algorithm, which produced a 23.16% rate of misidentification of $Z \to c\bar{c}$ events and a 1.74% rate of misidentification of $Z \to q'\bar{q}'$ events, with $q' \equiv (u, d, s)$, for an 80% efficiency of accurate identification of the $Z \to b\bar{b}$ events. The other algorithm, inspired by the techniques presented in the LCFIPlus framework, developed for future e^+e^- linear colliders like the International Linear Collider (ILC), classifies events into four categories through secondary vertex reconstruction, with each category representing the majority of decay events to a certain hadronic flavour.

Contents

1 Introduction

The Higgs boson was discovered at the Large Hadron Collider in 2012. After this discovery, the priority in high-energy physics experiments is to study the Higgs boson and make precise measurements to test if it follows the Standard Model. The dominant decay mode of Higgs boson is to bottom quark-antiquark pair. It also has appreciable branching fractions to other hadronic decay channels. Thus, it is essential in the study of the Higgs boson to be able to distinguish between these different hadronic event signatures.

With the advent of high energy future e^+e^- colliders, identifying decays to charm quark has also become a target of study. The identification of decay events to charm quark helps us to study the complete hadronic decay spectrum of the Higgs boson along with the flavour-changing neutral currents in the top sector.

One of the experimental challenges in studying the Higgs boson is to identify and separate these hadronic decay modes. All of these hadrons, however, have certain quantitative and distinguishable properties that can be measured in a detector. It is the aim of this thesis to present and review some flavour identification algorithms in the settings of a circular collider, specifically in the context of the IDEA detector concept of FCC-ee.

The bottom hadrons have sizable and longer lifetimes than the charm and the light hadrons, with the exception of strange hadrons. As a consequence of this, the particles originating from the bottom hadron decays have larger transverse impact parameters with respect to the primary vertex compared to those for

the particles originating from the charm or the light hadron decays. This forms the basis of the impact parameter tagging algorithm.

As a result of the sufficient lifetimes of the bottom and the charm hadrons, in the events with the Higgs boson decaying to a bottom or a charm hadron pair, one or more decay vertices are present. They are far enough from the interaction point for it to be possible to distinguish and find them. If there are more than one charged particle tracks originating from a decay vertex, these charged particle tracks can be re-fitted to find that decay vertex. The bottom quark decays to a charm quark with a large branching fraction and the charm quark decays further, dominantly to lighter quarks. Due to these cascading decays, the bottom hadrons have longer decay chains than the charm hadrons, giving rise to multiple decay vertices. This can be used to categorise the bottom, the charm, and the light hadron events. The charm hadrons, having smaller masses and shorter lifetimes compared to the bottom hadrons, are more challenging to identify.

The jets containing bottom hadrons can be identified by using furthermore parameters. The hadrons containing the bottom quark have significantly higher mass than hadrons containing the charm or the light quarks because the bottom quark is heavier compared to these quarks. Therefore, the particles originating from the bottom hadron decays have higher relative momenta transverse to their corresponding jet axes than those originating from the charm or the light hadron decays. This property of the bottom hadrons gives rise to the soft-lepton taggers.

1.1 System of Units

Although the S.I. units are very reasonable when used in everyday life, it is not logical to use them in the world of particle physics. In high-energy physics, the system of natural units is used to measure the properties of the particles. This thesis follows the same system of units.

In particle physics, energy is measured in GeV and the speed of light, c, and the reduced Planck's constant, $\hbar$, are assigned unit values, i.e.,

$$c = \hbar = 1.$$

Property		Unit
Energy	:	GeV
Momentum	:	GeV
Mass	:	GeV
Time	:	GeV^{-1}
Length	:	GeV^{-1}

Unless explicitly specified, all quantities in this thesis are expressed in natural units.

2 Standard Model of Particle Physics

Studying particle physics plays an essential part in our quest to understand the laws of nature. Particle physics is concerned with the elementary particles, which are the fundamental constituents of the Universe, and the interactions between them. The Standard Model of particle physics embodies our current understanding of these fundamental particles and their interactions. It provides a unified account where the forces or interaction between particles themselves are described by the exchange of particles. The Standard Model provides a successful description of all current experimental data and represents one of the most remarkable triumphs of modern physics.

2.1 Fundamental Particles

Everything in the Universe, including the world around us, appears to be formed from just a few different particles. Atoms, which were once considered unbreakable, are the bound states of negatively charged electrons which orbit around a central nucleus composed of positively charged protons and electrically neutral neutrons. The electrons are bound to the nucleus due to the electrostatic attraction between their opposite charges. This attraction is the low-energy manifestation of the fundamental theory of electromagnetism, known as Quantum Electrodynamics. The atomic nucleus consists of the protons and neutrons that are bound together by the strong nuclear force, which is a manifestation of the fundamental theory of strong interactions, called Quan-

tum Chromodynamics. The third fundamental interaction of particle physics is the weak force, which is responsible for the nuclear β-decays observed in certain radioactive isotopes and the nuclear fusion processes like the ones that power the Sun. In both nuclear β-decay and nuclear fusion, a nearly massless particle, the electron neutrino, is produced. Most of the physical phenomena encountered regularly can be described in terms of the electron, electron neutrino, proton, and neutron, interacting by the electromagnetic, strong, and weak forces. This picture is completed by the gravitational interaction, which although extremely weak, is always attractive. Gravity is responsible for large-scale structure of the Universe. This physical model with only four fundamental particles and four fundamental interactions is very simple and appealing. However, upon probing at higher energy scales, further structure is observed. The protons and neutrons are not elementary particles but are the bound states of what are currently believed to be genuinely fundamental particles called quarks. In the proton two up-quarks and a down-quark, and in the neutron two down-quarks and an up-quark are held together by strong interactions.

Collectively the electron, the electron neutrino, the up-quark, and the down-quark form what is known as the first generation. As far as we know, they are not composite but truly elementary particles and represent the basic building blocks of the low-energy Universe. However, when particle interactions are studied at higher energy scales like encountered in particle colliders, further complexity is revealed.

For each of the four particles in the first-generation, there are exactly two more copies that differ only in their masses. These additional eight particles form what are known as the second and third generations. The second-generation muon is essentially a heavier version of the electron with the same charge but mass $m_\mu \approx 200 m_e$, and the third-generation tau-lepton is an even heavier copy with mass $m_\tau \approx 3500 m_e$. Apart from having different masses, which have physical consequences, the properties of the electron, muon, and tau-lepton are the same to current experimental precision in the sense that they undergo the same fundamental interactions.

There is strong experimental evidence that there are no further generations of particles but the aforementioned three; hence the matter content of the Universe appears to be in the form of the twelve fundamental spin-half particles

listed in Table 2.1. The spin is an intrinsic property of a particle; particles with an integer spin are called bosons and the particles with a half-integer spin are called fermions. Apart from the neutrinos, the masses of which are very small and not yet known, the masses of the particles are found to increase from generation to generation as can be observed in Table 2.1. It is generally believed that there is some underlying reason for this pattern of masses, but it is not currently understood.

	Leptons			Quarks		
	Particle	Q	Mass/GeV	Particle	Q	Mass/GeV
First	Electron (e^-)	-1	0.0005	down	$-1/3$	0.005
generation	Neutrino (ν_e)	0	$<10^{-9}$	up	$+2/3$	0.002
Second	Muon (μ^-)	-1	0.106	strange	$-1/3$	0.1
generation	Neutrino (ν_μ)	0	$<10^{-9}$	charm	$+2/3$	1.3
Third	Tau (τ^-)	-1	1.78	bottom	$-1/3$	4.5
generation	Neutrino (ν_τ)	0	$<10^{-9}$	top	$+2/3$	173

Table 2.1: The twelve fundamental fermions divided into leptons and quarks [1].

The Dirac equation of relativistic quantum mechanics describes the dynamics of each of the twelve fundamental fermions. One important consequence of the Dirac equation is that for each of the twelve fermions there exists an antiparticle state with exactly the same mass, but opposite quantum numbers, including charge. Antiparticles are denoted either by their charge or by a bar over the corresponding particle symbol. For example, the anti-electron, also called the positron, is denoted by e^+, and the anti-up-quark by $\bar{u}$.

2.1.1 Quarks and Leptons

The fundamental particles interact with each other through the four fundamental forces, namely gravitation, electromagnetism, the strong force, and the weak force. The gravitational force, which is experienced by every massive object in presence of another massive object, is extremely small between two elementary particles and can be neglected in the discussion of particle interactions. The properties of the twelve fundamental fermions are categorised by the types of interaction among the remaining three that they experience. It is summarised in Table 2.2.

All of the twelve particles undergo weak interaction. With the exception of the electrically neutral neutrinos, the other nine particles are electrically charged

					strong	electromagnetic	weak
Quarks	down-type	d	s	b	✓	✓	✓
	up-type	u	c	t			
Leptons	charged	e^-	μ^-	τ^-		✓	✓
	neutrinos	ν_e	ν_u	ν_τ			✓

Table 2.2: The forces experienced by different fundamental particles [2].

and hence participate in the electromagnetic interaction of QED. Only the quarks carry the QCD equivalent of electric charge, called the colour charge. Consequently, only the quarks experience strong interaction. Quarks are never observed as free particles because of the nature of the QCD interaction. So they are always confined to bound states called hadrons, such as the proton and the neutron. Therefore, in high-energy particle reactions, quarks are always observed in the form of hadron jets, which are created by the process known as hadronisation. Only the quarks undergo the strong interaction, which distinguishes them from the electron, muon, tau-lepton, and the neutrinos, which are collectively referred to as the leptons.

2.2 Fundamental Interactions

In classical electromagnetism, the electrostatic force between charged particles is described in terms of a scalar potential. This classical description of a force arising from a potential is unsatisfactory for several reasons. For example, when an electron scatters in the electrostatic potential of a proton, there is a transfer of momentum between the two charged particles without any apparent mediating body.

In modern particle physics, each force is described by a Quantum Field Theory. The QFT of electromagnetism is known as the theory of Quantum Electrodynamics, where the interactions between charged particles are mediated by the exchange of virtual photons; the term virtual is used because these photons do not follow the relativistic energy-momentum relation. Describing a force in terms of particle exchange alleviates the need to invoke any mysterious action at a distance. As an example, Figure 2.1 shows the interaction between two electrons by the exchange of a photon. In the first diagram, the upper electron emits a photon, which at a later time is absorbed by the lower electron. The effect of this interaction is to transfer momentum from one electron to the

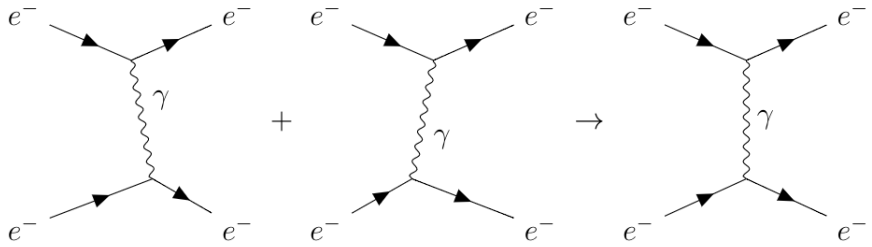

Figure 2.1: The scattering of two electrons in QED by the exchange of a photon. The first two diagrams show the two possibilities of the interaction, with time flowing from left to right. The third diagram shows the Feynman diagram of the interaction, representing the combined effect of the interaction.

other, and it is this transfer of momentum which manifests itself as a force. The second diagram shows the other possible time-ordering of the interaction with the lower electron emitting the photon that is subsequently absorbed by the upper electron. Since the exchanged particle is not observed, only the combined effect of these two time-ordered diagrams is physically meaningful, which is represented in the third diagram. Such diagrams are very useful for calculating the strength of the interaction and the consequential effects of the interaction, and they are called Feynman Diagrams.

Particle	Q	Mass/GeV	Spin
Photon (γ)	0	0	1
Gluons (g)	0	0	1
Charged weak bosons ($W^{\mp}$)	∓ 1	80.379	1
Neutral Weak Boson (Z)	0	91.188	1
Higgs Boson (H)	0	125.18	0

Table 2.3: The vector gauge bosons and the scalar Higgs boson of the Standard Model [1].

Each of the three interactions relevant in particle physics is described by a QFT corresponding to the exchange of a spin-1 force-carrying particle, known as a gauge boson. The massless photon, as seen in the interaction described above, is the gauge boson of QED. In the case of the strong interaction, described by Quantum Chromodynamics, the force-carrying particles are called gluons which are also massless. The weak charged-current interaction is mediated by the charged W^+ and W^- bosons. The weak neutral-current interaction, closely related to the charged-current interaction, is mediated by the electrically neutral Z boson. Properties of these bosons are shown in Table 2.3.

2.3 Higgs Boson

The final element of the Standard Model is the Higgs boson. It was discovered by the ATLAS and CMS experiments at the Large Hadron Collider (LHC) in 2012. The Higgs boson, with a mass of 125 GeV, differs from all the other Standard Model particles. Unlike the fundamental fermions and the gauge bosons, which are respectively spin-half and spin-1 particles, the Higgs boson is a spin-0 scalar particle. As conceived in the Standard Model, the Higgs boson is the only fundamental scalar particle ever discovered.

The Higgs boson plays a special role in the Standard Model; it arises from the mechanism, known as the Higgs mechanism, by which all other particles acquire mass. Without it all the particles would be massless and, like photons, would propagate at the speed of light. In QFT, the Higgs boson can be thought of as an excitation of the Higgs field. Unlike the fields associated with the other Standard Model particles, which have zero vacuum expectation values, the Higgs field in the Standard Model Higgs mechanism has a non-zero vacuum expectation value. It is the interaction of the initially massless particles with this non-zero Higgs field that gives them their masses. The discovery of a Higgs-like particle at the LHC represented a remarkable validation of the theoretical ideas which constitute the Standard Model. The subtle mathematical details of the Higgs mechanism are discussed in the next section. The masses of the weak gauge bosons, $W^{\mp}$, Z, and the Higgs boson are all of the order of 100 GeV, known as the electroweak scale. This is not a coincidence; in the Standard Model, the masses of the weak gauge bosons are intimately connected to the Higgs mechanism.

2.4 Higgs Mechanism

In the Standard Model, particles acquire masses through their interactions with the Higgs field. The description of the Higgs mechanism, presented in this section, follows the pedagogical approach presented in Modern Particle Physics by Mark Thomson[2].

The mass terms for a real scalar field can arise from a broken symmetry. A Lagrangian consists of two parts, a kinetic term involving the derivatives of

the fields and a potential term expressed in terms of the fields themselves. For a scalar field ϕ with the potential,

$$V(\phi) = \frac{1}{2}\mu^2\phi^2 + \frac{1}{4}\lambda\phi^4, \tag{2.1}$$

the corresponding Lagrangian is given by,

$$\begin{aligned} \mathcal{L} &= \frac{1}{2}(\partial_\mu\phi)(\partial^\mu\phi) - V(\phi), \\ &= \frac{1}{2}(\partial_\mu\phi)(\partial^\mu\phi) - \frac{1}{2}\mu^2\phi^2 - \frac{1}{4}\lambda\phi^4. \end{aligned} \tag{2.2}$$

The term $\frac{1}{2}(\partial_\mu\phi)(\partial^\mu\phi)$ in 2.2 can be associated with the kinetic energy of the scalar particle and a term quadratic in ϕ, here $\frac{1}{2}\mu^2\phi^2$, can represent the mass of the particle. The ϕ^4 term can be identified as self-interactions of the scalar field, corresponding to a four-point interaction vertex.

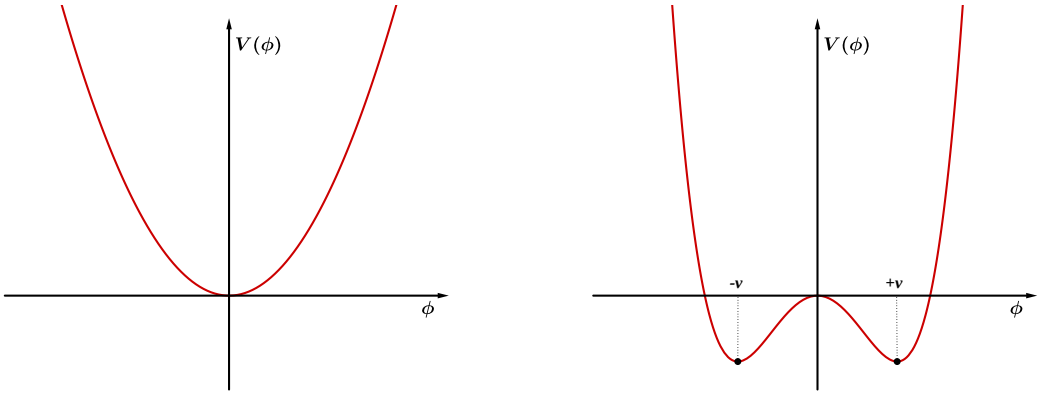

(a) $\mu^2 > 0$ **(b)** $\mu^2 < 0$

Figure 2.2: The one-dimensional potential $V(\phi) = \mu^2\phi^2/2 + \lambda\phi^4/4$ for $\lambda > 0$ and the cases where $\mu^2 > 0$ and $\mu^2 < 0$ respectively.

The vacuum state is the lowest energy state of the field ϕ and corresponds to the minimum of the potential. For the potential to have a finite minimum, λ must be positive. If μ^2 is also chosen to be positive, the resulting potential, shown in Figure 2.2a, has a minimum at $\phi = 0$. In this case, the vacuum state corresponds to the field ϕ being zero and the Lagrangian represents a scalar particle with mass μ and a four-point self-interaction term proportional to ϕ^4. However, whilst λ must be greater than zero for there to be a finite minimum, there is no such restriction for μ^2. If $\mu^2 < 0$, the associated term in

the Lagrangian can no longer be interpreted as a mass and the potential has minima at,

$$\phi = \pm v = \pm \left| \sqrt{\frac{-\mu^2}{\lambda}} \right|, \tag{2.3}$$

as shown in Figure 2.2b. For $\mu^2 < 0$, the lowest energy state does not occur at $\phi = 0$ and the field is said to have a non-zero vacuum expectation value v. Since the potential is symmetric, there are two degenerate possible vacuum states. The actual vacuum state of the field either will be $\phi = +v$ or $\phi = -v$. The choice of the vacuum state breaks the symmetry of the Lagrangian, a process known as spontaneous symmetry breaking.

A similar mechanism follows in the case of a complex scalar field of the form,

$$\phi = \frac{1}{\sqrt{2}}(\phi_1 + i\phi_2), \tag{2.4}$$

but the potential is two-dimensional. In the Higgs mechanism, the spontaneous symmetry breaking of a complex scalar field is embedded in a theory with a local gauge symmetry. The Lagrangian is required to be invariant under this local gauge symmetry, therefore covariant derivatives are used in place of partial derivatives. If the local gauge symmetry is $U(1)$, then after the spontaneous symmetry breaking, the resulting Lagrangian represents the massive Higgs boson, a massive gauge boson, the interaction of the gauge field with the Higgs field, and the self-interactions of the Higgs field. The scale for the masses of both the gauge boson and the Higgs boson are set by the vacuum expectation values of the scalar field.

The local gauge symmetry of the Standard Model is $U(1)_Y \times SU(2)_L$. Because the Higgs mechanism is required to generate the masses of the electroweak gauge bosons, W^-, W^+, and Z, one of the scalar fields must be neutral, written as ϕ^0, and the other must be charged such that ϕ^+ and $(\phi^+)^* = \phi^-$ give the longitudinal degrees of freedom of the W^+ and W^-. The Higgs field consists of two scalar fields in a weak isospin doublet,

$$\phi = \begin{pmatrix} \phi^+ \\ \phi^0 \end{pmatrix} = \frac{1}{\sqrt{2}} \begin{pmatrix} \phi_1 + i\phi_2 \\ \phi_3 + i\phi_4 \end{pmatrix}. \tag{2.5}$$

Hence it has four compontents. The Glashow-Salam-Weinberg model along with the Higgs mechanism not only predicts three massive gauge bosons and

a massive scalar boson but also gives a relation between the electromagnetic and weak couplings. From the known values of the mass and the coupling of the weak bosons $W^{\mp}$, the vacuum expectation value of the Higgs field is found to be $v = 246$ GeV.

The spontaneous symmetry breaking that gives rise to the masses of $W^{\mp}$ and Z bosons, can also be used to generate the masses of the fermions. The interactions of the fermions with the Higgs field are also known as Yukawa interactions. The coupling of these interactions is not given by the Higgs mechanism but can be chosen to be consistent with the observed masses of the fermions.

2.5 Standard Model Higgs Boson

The standard model Higgs boson is an electrically neutral scalar particle. Its mass is a free parameter of the Standard Model, given by $m_H = 2\lambda v^2$. The Higgs boson interacts with all the fermions with a coupling strength proportional to the fermion mass. Therefore, it can decay via $H \to f\bar{f}$ for all kinematically allowed decay modes with $m_H > 2m_f$. It can also decay via $H \to WW^*$ or $H \to ZZ^*$, where * indicates that one of the particles is virtual. The dominant processes through which the Higgs boson is produced and decays are determined by the proportionality of the Higgs boson couplings to mass. The coupling of the Higgs boson to a particle with mass m is proportional to their mass, therefore the partial decay width, i.e. the probability of the Higgs boson decaying to that particle is proportional to m^2. Hence it decays preferentially to the more massive particles that are kinematically accessible, the largest branching ratio being to a bottom quark-antiquark pair. The branching fractions of the Higgs boson are given in Table 2.4.

Prior to the turn-on of the Large Hadron Collider at CERN, the window to find a Standard Model Higgs boson was relatively narrow. The absence of a signal from the direct searches at LEP indicated that $m_H > 114$ GeV[3]; while the limits on the size of the quantum loop corrections from the precision electroweak measurements at LEP and the Tevatron suggested that $m_H \leq 150$ GeV and that m_H was not likely to be greater than 200 GeV[4]. One of the main aims of the LHC was the discovery of the Higgs boson, assuming it existed.

Decay mode	Branching ratio
$H \to b\bar{b}$	57.8%
$H \to WW^*$	21.6%
$H \to \tau^+\tau^-$	6.4%
$H \to \mathrm{gg}$	8.6%
$H \to c\bar{c}$	2.9%
$H \to ZZ^*$	2.7%
$H \to \gamma\gamma$	0.2%

Table 2.4: Predicted branching ratios of the Higgs boson.[1]

In 2012, the ATLAS and the CMS experiments at LHC announced the discovery of a new particle compatible with the Standard Model Higgs boson. ATLAS[5] and CMS[6] recorded an excess of events around a mass of 125 GeV compared to the expected background in the distribution of the reconstructed invariant mass of two photons in candidate Higgs events for the process $H \to \gamma\gamma$. They observed a similar excess in the four-lepton candidate events of the process $H \to ZZ^* \to 4\ell$.

In the eight years after the discovery of the Higgs boson, measurements of many of its properties, like its production cross sections in multiple channels, several decay branching fractions, and spin, have been found to be compatible with the Standard Model predictions. But further studies are required. Supersymmetry, which is a possible extention to the Standard Model, gives rise to five physical Higgs bosons[7]. Further high-precision measurements of the Higgs boson can elucidate the possibility of the existence of more Higgs like bosons. Furthermore, it is currently not known whether the observed Higgs boson is a fundamental scalar particle or a composite. The high-precision measurements of the spin and branching ratios of the Higgs boson will further test the predictions of the Standard Model. Perhaps more importantly, a detailed understanding of all the properties of the Higgs boson and their deviations, if any, from the Standard Model predictions may well shine some light on what lies beyond the Standard Model, if anything.

3 Particle Colliders

Particle colliders are machines that use electromagnetic fields to propel subatomic charged particles to very high velocities and energies and collide them at specific interaction points. The individual interactions produced by the colliding particle beams are referred to as events. The detectors, positioned around the interaction points, employ a multitude of technologies to measure the properties of the particles produced in these events with the aim to reconstruct the primary reaction undergone by the particles at the interaction point, as represented by a Feynman diagram.

The most common types of particle colliders are electron-positron and proton-(anti)proton colliders. This distinction, as the names suggest, is based on the initial particles which are collided at high energies in such colliders. Since electrons are elementary point particles, their collisions are clean and amenable to high precision measurements. However, because they are light, their collisions can not reach similar energies attainable by using heavier particles. Protons are composite particles and are nearly 2000 times more massive than electrons.

At the Large Hadron Collider[8], the number of Higgs bosons produced is a tiny fraction of the total interactions taking place inside the detectors. Because it is a proton-proton collider, the production rate of QCD multi-jet final states is considerably higher (about $\mathcal{O}(10^9)$ higher) than that of electroweak processes including the production of the Higgs boson. This makes it challenging to distinguish the events with the Higgs boson producing hadron jets as final states from the QCD background. At the same time, the initial state of particles is not known for individual events. On the other hand, in electron-positron

colliders like the Large Electron-Positron collider[9], the incoming particles undergo electroweak interaction and have no background from QCD production process and since the incoming particles are elementary particles with precisely known energy and momentum, the initial state of the interaction is completely defined. This significantly enhances the amount of information that can be extracted from the observed events, therefore they are complementary to proton-(anti)proton colliders for high-precision measurements of the Higgs boson.

Particle colliders are also categorised based on their shape; they can either be linear or circular. proton-(anti)proton colliders are always circular but e^+e^- can either be circular or linear. High energy accelerators collect particles in bunches and then collide these bunches together but very few of the particles in the bunches actually collide in each bunch crossing. In a circular collider, like LEP, these bunches travel around a roughly circular ring in opposite directions and therefore can be collided many times (about 10^{10} times) before the beams are eventually dumped, which facilitates a high rate of collision and allows for the collection of high statistics data samples. This is advantageous for high precision measurements. At the same time, there can be more than one interaction points in a circular collider, and therefore more than one detector. The particles, however, lose energy due to the synchrotron radiation, which has to be compensated for. Synchrotron radiation is the electromagnetic radiation emitted by charged particles when they are accelerated radially, i.e. in the direction perpendicular to their direction of travel. Since the energy loss due to this rises with the fourth power of the particle energy and can only be mitigated by increasing the radius of the accelerator, it is impractical to build an e^+e^- collider for energies higher than 400-500 GeV. In linear colliders, the particles do not lose energy through the synchrotron radiation, since they travel in straight lines, therefore they can reach higher center-of-mass energies. Though, the bunches cannot be reused, which makes it more difficult to collect high-statistics data samples.

3.1 Proposed Electron-Positron Colliders

With a 27 km long circumference, the Large Electron-Positron collider is the largest electron-positron collider ever built. While LEP was a circular collider,

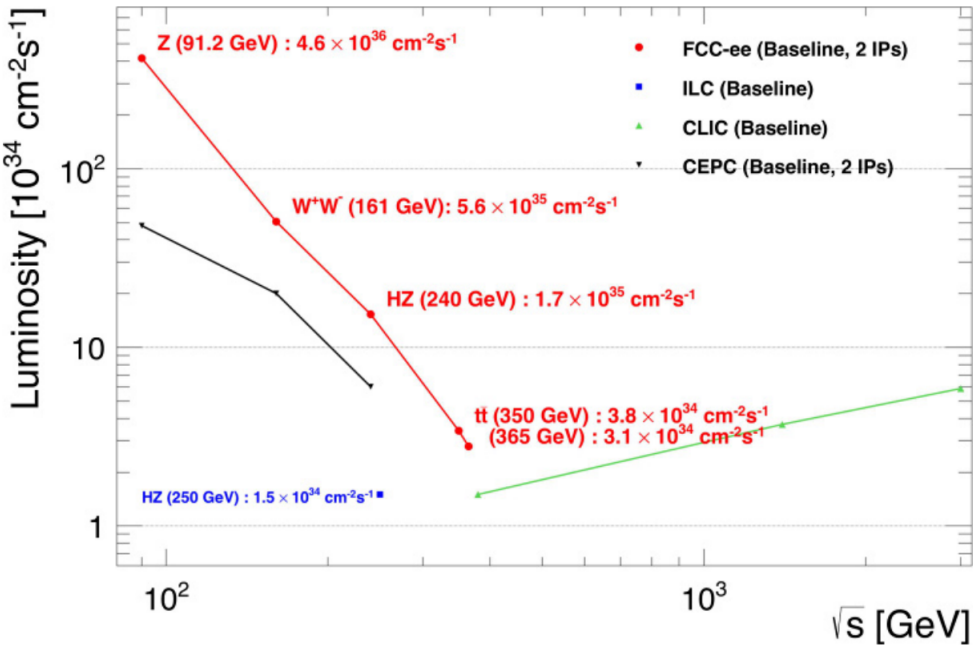

Figure 3.1: Luminosities expected at the proposed e^+e^- colliders as a function of center-of-mass energy.[11][12][13][14]

the Stanford Linear Collider[10], with a length of 3.2 km is the only linear collider ever built. Presently, LHC, which is hosted in the tunnel that LEP previously occupied, is the largest functioning collider. Plans have been proposed to build bigger e^+e^- colliders. The main focus of such projects is on Higgs Factories, i.e. e^+e^- colliders that are able to produce $\mathcal{O}(10^6)$ Higgs events in a clean environment. The various proposed projects also have additional focii; whearas for linear colliders, these are mainly on higher energies, where complimentary precision measurements can be done and the "New Physics" be potentially discovered, for circular colliders, these are on the energies where the known electroweak bosons and the top quark can be studied with an unprecedented precision. The extremely high rates of produced events also provides sensitivity to exceedingly rare processes. Currently it is not known whether the "New Physics", if it exists, is at higher energies or at lower couplings. Two linear e^+e^- colliders have been proposed. The first is the International Linear Collider[15], to be built in Japan. It was originally designed to have a collision energy of 500 GeV that has now been re-optimised after the discovery of the relatively light Higgs boson, to 250 GeV, with a possibility to be upgraded in two steps to 500 GeV and 1 TeV, respectively. It will be between 30 and 50 km long, more than 10 times longer than SLC. The other proposed linear collider is Compact Linear Collider[16],

which is planned to be built and operated in three stages with collision energy reaching up to 3 TeV. At its lowest center-of-mass energy of 380 GeV, it will function as a Higgs factory.

There have also been proposed two circular e^+e^- colliders, which are virtually identical in design. Circular e^+e^- colliders excel at high-precision measurements because they can attain higher luminosities than the proposed linear colliders. The Circular Electron-Positron Collider, with a circumference of 97.5 km, is intended to be built in China. It is planned to be operated as a Higgs factory for the most part; it is also planned to be run at the Z boson peak for precision measurements of the Z boson mass and its couplings.

At CERN, a post-LHC circular collider has been proposed, which is called the Future Circular Collider. This proton-proton collider is planned to reach a center-of-mass collision energy of at least 100 TeV. The first step of this collider project is FCC-ee, which is a proposed e^+e^- collider, designed to operate at the center-of-mass collision energies between 90 and 365 GeV.

Figure 3.1 shows the luminosities expected at the four proposed e^+e^- colliders.

3.1.1 FCC-ee

Initially conceptualised as a stand-alone project[17], FCC-ee[11] is now the phase-1 of the FCC Integral Project. It offers the highest luminosities among all the conceived future electron-positron colliders for the center-of-mass energies from 90 to 365 GeV. FCC-ee is proposed to operate at the Z pole for 4 years, at the W^+W^- threshold for 2 years, as a Higgs factory at the center-of-mass energy of 240 GeV, dominantly producing the Higgs boson through the Higgs-strahlung process for 3 years, at the top quark production threshold for 1 year, and at and above the $t\bar{t}$ threshold for 5 years with the center-of-mass energy of $350 - 365$ GeV. It is supposed to have two to four interaction points and the detectors planned to be installed at these points are being developed, so far, as CLD and IDEA detector concepts.

FCC-ee not only has the potential for high-precision measurements, which will test the Standard Model at a higher scale than done before or lead to the new

physics, but it can also be the source of direct discoveries of the missing pieces in the Standard Model like right-handed neutrinos, dark matter particles, or new very-weakly-coupled particles. This sensitivity to new particles is made possible by the unprecedented number of particle decays in a very clean environment of FCC-ee; 5×10^{12} Z bosons, out of which 1.5×10^{12} bottom decays and 3×10^{11} τ decays.

4 Higgs Physics at e^+e^- Colliders

Being the latest discovered Standard Model particle, the Higgs boson is the least understood of all. The high-luminosity upgrade at LHC will further improve the accuracy of the measurements of its properties[18]. A precision, which is qualitatively up to the 1-2% level on the Higgs-Yukawa coupling is expected to be achieved, although under a number of model-dependent assumptions, particularly on the decays of Higgs boson which are not directly accessible in a hadron collider. Lepton colliders like FCC-ee provide an opportunity to make direct model-independent observations. Sub-percent accuracies are required on the coupling measurements of the Higgs boson since most of the Standard Model extensions predict deviations in Higgs coupling at such scale. The quantum corrections to the Higgs boson couplings are also at the level of a few percent. The measurements of the Higgs boson properties have to be pushed well below this precision level. An experimental sample of at least one million Higgs bosons needs to be produced and analysed to potentially achieve this statistical precision.

4.1 Production Processes

At electron-positron colliders, Higgs boson production proceeds mainly via two processes: the Higgs-strahlung process and WW fusion. The Feynman diagrams of the two processes are shown in Figure 4.1. In the Higgs-strahlung process $e^+e^- \rightarrow HZ$, the electron and the positron annihilate to create a

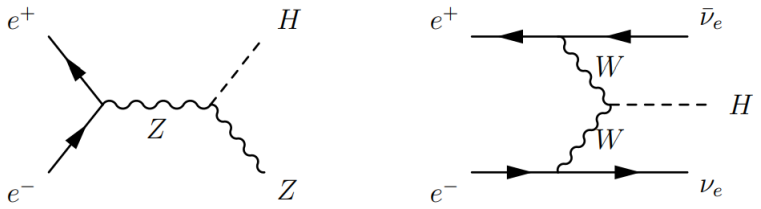

Figure 4.1: The dominant production processes at e^+e^- colliders.

virtual Z boson. This highly-energetic virtual Z boson can then emit a Higgs boson. In the WW fusion process $e^+e^- \to (WW \to H)\nu\bar{\nu}$, the electron and the positron interact weakly by emitting $W^\mp$ bosons, which fuse to produce a Higgs boson.

The production amplitudes for these two processes interfere if the Z boson in the Higgs-strahlung process decays to an electron neutrino-antineutrino pair. It turns out that this interference term is positive and has the same amplitude as that for the individual processes in this cross-over region between these two processes. Thus this interference adds to the rate to which the WW-fusion process will be used at the FCC-ee.[19]

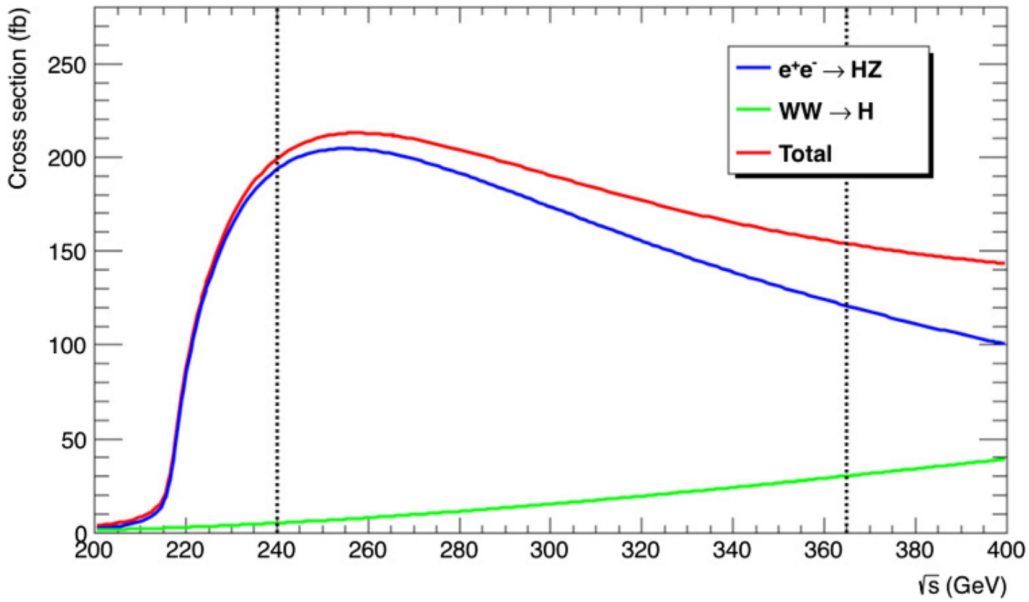

Figure 4.2: The cross-section of the dominant production processes of the Higgs boson as a function of center-of-mass energy.[11]

Figure 4.2 presents the cross-section as a function of the center-of-mass energy for the two processes. The total cross-section maximises at the center-of-mass energy of 260 GeV, but as a consequence of the specific luminosity profile of a circular collider, the event rate is highest at the center-of-mass energy of

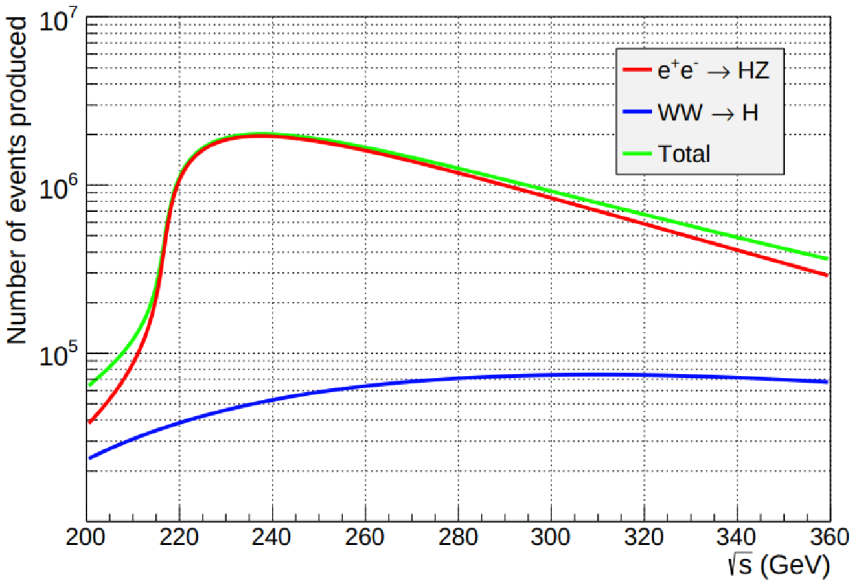

Figure 4.3: Number of produced events via the dominant production processes of the Higgs boson as a function of center-of-mass energy.[17]

240 GeV, as shown in Figure 4.3. The event sample at 240 GeV is dominated by the HZ events generated from the Higgs-strahlung process. Since the cross-section at 240 GeV is around 200 fb, to produce one million events, an integrated luminosity of 5 ab^{-1} is required. This sample is complemented by 180,000 HZ events and 45,000 WW-fusion events collected at the center-of-mass energy of 365 GeV.[11]

4.2 Analysis Strategy

Since the Higgs-strahlung process, $e^+e^- \to HZ$, is the dominant production process in e^+e^- colliders at 240 GeV, the analysis strategy reported below corresponds to this process.

To count Higgs boson events, the invariant mass of the final state fermions, $f\bar{f}$ $(f = e^-, \mu^-, q)$, from the Z boson decay is calculated from their measured four-momenta and is required to be consistent with the Z boson mass. The mass recoiling to this system of Z boson decay products is then measured and the events with the recoil mass compatible with the Higgs boson mass are counted. The events with this recoil mass within a range around the Higgs boson mass can be tagged as Higgs events. This unbiased sample of Higgs events can be used to measure the branching ratios of the decay modes of the

Higgs boson. This sample of events can be divided, based on the signatures in the detector, into different decay modes of the Higgs boson, like $\tau^+\tau^-$, $\mu^+\mu^-$, $q\bar{q}$, $\gamma\gamma$, gg, etc. and the branching ratios of the Higgs boson can be measured.

This sample of events is easily accessible experimentally for the events with the Z boson decaying to e^+e^- or $\mu^+\mu^-$, as these events leave very clean signatures. Therefore these events can be used to measure the cross-section of the Higgs-strahlung process, HZ, without model-dependent assumptions. This measurement is a direct probe of the HZZ coupling, g_{HZZ}. Since the Higgs-strahlung process is the dominant process of Higgs boson production at the collision energy of 240 GeV, the precision of all other couplings is limited by the accurate measurement of this cross-section. To identify these events, those with an oppositely charged lepton pair of the same flavour are selected and the invariant mass of the lepton pair, including close-lying photons from final-state radiation, is required to be compatible with the Z boson mass.[20][17]

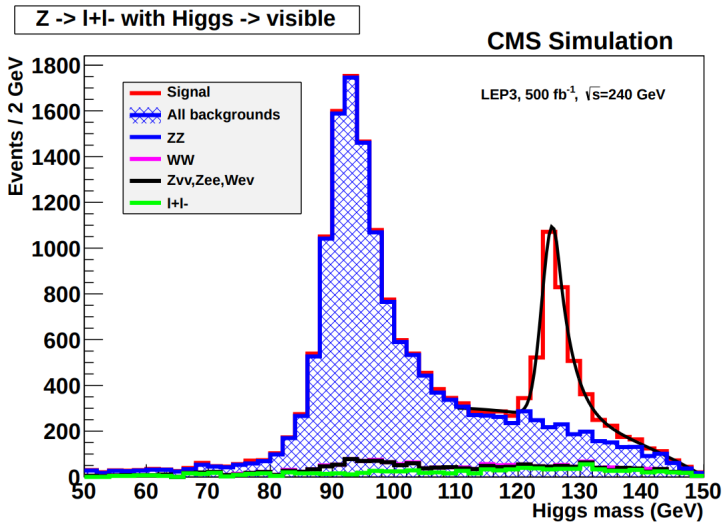

Figure 4.4: Distribution of the visible mass recoiling against the lepton pair in candidate HZ events with $Z \to \ell^+\ell^-$ for HZ signal and all background. The recoiling mass is required to be visible, i.e. consist of two reconstructed "jets" (These "jets" may contain only one particle above the detection threshold).[20]

The Higgs boson mass can be extracted from the distribution of the mass recoiling against the lepton pair from the Z boson decay, as shown in Figure 4.4. This analysis also reduces the uncertainty on the Higgs mass remarkably. An early FCC-ee (called TLEP at the time) study indicated statistical precision of

53 MeV based on an event sample one-tenth of what is now expected[17]. A later CEPC study points to a precision of 5.9 MeV[21].

Events, where the Z boson decays leptonically, can also be used to measure the branching fraction of the invisible decays of the Higgs boson. This would include the Higgs boson potentially decaying to a neutrino-antineutrino pair or a pair of any dark matter candidate particles.

4.2.1 Higgs Boson Decay Width

In the Standard Model, the total decay width of the Higgs boson is only 4 MeV, therefore it is not possible to directly measure it in e^+e^- collisions. But the decay width of the Higgs boson decaying to a Z boson pair can be used to measure the total width because the total width of the Higgs boson is related to its decay width to a Z boson pair by:

$$\Gamma_{tot} = \frac{\Gamma(H \to ZZ)}{BR(H \to ZZ)}. \tag{4.1}$$

Since the partial decay width $\Gamma(H \to ZZ)$ is directly proportional to the cross-section σ_{HZ}. Therefore, as a consequence of the precise measurement of this cross-section, the total decay width of the Higgs boson can be measured with a precision of the order of 1.3% from this channel[11].

Measurement of all statistically available decay modes of the Higgs boson are being aimed and sub-percent precision is expected on the partial decay widths of the dominant decay modes of the Higgs boson; precision of 0.3% for $H \to b\bar{b}$ channel and 0.9% for $H \to \tau^+\tau^-$ channel, 1.2% for $H \to W^+W^-$ channel[11].

4.3 Need for Flavour Identification

There are four dominant decay modes that result in hadronic final states: $b\bar{b}$, $c\bar{c}$, gg, and some fraction of WW^*. The portion of events with WW^* final state can possibly be separated significantly based on the jet count and some constraints on the invariant mass of jet pairs. To distinguish and identify the

other three final states, flavour identification techniques are required that exploit the distinguishing features of these particles.

Among these final-state particles, the bottom and the charm quark have non-negligible lifetimes. The gg- final state is likely to leave signatures similar to light quarks (u, d, s). The study reported in this thesis was only performed for the $q\bar{q}$ final states and does not show results corresponding to the gg- final state.

5 Detectors

Modern particle physics detectors are large and layered structures composed of multiple detector elements, which are used to measure the properties of particles passing through them like, their charge, trajectory, momentum, energy etc.

For FCC-ee, two complementary detector designs are being studied as CLIC-Like Detector or CLD[22], which has been adapted to FCC-ee specifications from the most recent CLIC detector model[23], and International Detector for Electron-positron Accelerators or IDEA[11], which has specifically been developed for FCC-ee.

5.1 Generic Particle Detector

Typically, a detector consists of a cylindrical barrel centered around the beam-pipe at its axis. This cylindrical structure is closed by flat end caps on each side. Thus the detector can cover an almost complete solid angle, down to near the beam pipe.

Tracking Detector

The first part of the detector is dedicated to the tracking of charged particle trajectories. It detects the interaction of charged particles with sensitive detector elements at discrete points to measure their trajectory. The direction

and degree of curvature of the trajectory in the detector's magnetic field reveals, respectively, the charge and the momentum of the particle.

The innermost part of the tracking detector is devoted to very precise measurements of particles close to the interaction point. For this purpose, a vertex detector with a very fine spatial resolution is required. This is vitally important for vertex reconstruction, which is used, among other things, to identify the flavour of the hadronic decays.

Calorimeters

The tracking detector is surrounded by calorimeters where particles are stopped, leaving showers of secondarily produced particles. These showers are observed to measure the properties of the incoming particle, like their energy. The inner calorimeter, the electromagnetic calorimeter or ECAL, detects particles that interact electromagnetically including electrons and photons. It measures, both the amount of energy deposited by the particle and the location where the energy was deposited. The ECAL, in turn, is surrounded by the relatively larger hadronic calorimeter. The HCAL stops particles that interact strongly, i.e. hadrons, and measures their energy. Usually, it is not as precise as the ECAL, both in the energy measurement and the localisation.

Muon Chambers

Dedicated detectors, known as muon chambers, are situated outside the experiment to detect any penetrating muons. The muon, apart from the neutrinos, is the only particle that penetrates through the HCAL.

Solenoid

The detector also has a powerful solenoid electromagnet that produces a strong axial magnetic field, typically of the order of 1-4 Tesla. Charged particles follow curved trajectories in this magnetic field, which makes it possible to measure their charges and momenta.

At FCC-ee, the two beams cross at an angle of 30 mili-radians and therefore are at an angle of 15 mili-radians with respect to the axial magnetic field. This limits the magnetic field in the detectors to a maximum of 2 Tesla[11].

5.2 IDEA Detector Concept

The IDEA detector concept is one of the two detector concepts designed for FCC-ee. Figure 5.1 shows the schematic of this detector design. The beam pipe radius of FCC-ee is small with a thickness of 1.2 mm and 0.34% of X_0.

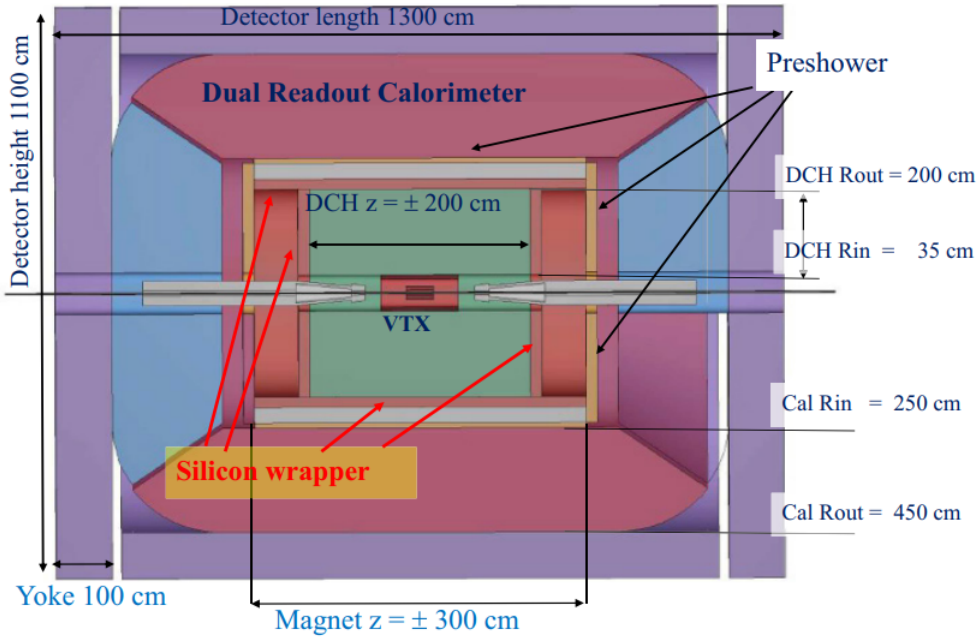

Figure 5.1: Schematic layout of the IDEA detector concept.[11]

The innermost detector, i.e. the IDEA vertex detector is a silicon pixel detector consisting of five layers with a thickness of 280 μm and 0.31% of X_0 per layer. The three inner vertex layers with 5 μm resolution are positioned at the radii 1.7 cm, 2.3 cm, and 3.1 cm respectively, and the two outer vertex layers are positioned at the radii 32 cm and 34 cm respectively.

The vertex layers are enclosed by the drift chamber, which is the IDEA tracking detector. This extremely transparent chamber, incorporating 112 layers of 100 μm resolution with a thickness of 14.8 mm per layer, is designed to provide high-precision momentum measurements and excellent particle identification. The main component of the gas in the drift chamber is Helium, thus it is very light and has very low multiple scattering. This results in an excellent momentum resolution, as demonstrated in Figure 6.3. The inner wall of this drift chamber is positioned at the radius 34.5 cm. It has a thickness of 0.2 mm

and 0.08% of X_0. The outer wall, with a thickness of 2 cm and 1.20% of X_0 is positioned at the radius 2.02 m.

The drift chamber is surrounded by a layer of silicon strip detectors, referred to as Silicon Wrapper, to provide a very precise space point measurement. It consists of two layers of thickness 470 μm and 0.52% of X_0 per layer, which are positioned at the radii 2.04 m and 2.06 m respectively

In the barrel region between the magnet and the calorimeter, a preshower detector is positioned. This arrangement allows for the accurate determination of the impact points of both the charged particles and the photons. It also further improve the tracking resolution.

The second preshower layer is surrounded by a lead-fiber dual-readout calorimeter. It is sensitive to the independent signals from the scintillation light and Cherenkov light production, which results in a good energy resolution for both electromagnetic and hadronic showers. Along with its intrinsic particle identification capabilities, the fine transverse granularity of the detector allows close showers to be separated, which provides good matching to track signals from the preshower detector and to muon track signals.

The dual-readout calorimeter is encompassed by the muon system. It consists of layers of chambers, which are embedded in the magnet return yoke.

6 Particle Tracks

Charged particles follow helical trajectories in the volume of the tracking detector due to the Lorentz force caused by the axial magnetic field generated by the solenoid coil. For a particle with charge Q moving with a velocity $\vec{v}$ in a magnetic field of strength B in the positive z direction, the Lorentz force can be written as,

$$\vec{F} = QB(\vec{v} \times \hat{z}). \tag{6.1}$$

Hence, the Lorentz force is perpendicular to the direction of motion of the particle in the (x, y)-plane, which will result in a circular motion in this plane. If the particle has a longitudinal component of momentum, then the motion of the particle will follow a helix.

A particle's helical trajectory can be defined by a set of parameters. There are multiple track representations that use different track parameters, which can describe the helical trajectory. The canonical representation is used for track fitting. In the canonical representation, five parameters describe the track's helical trajectory. Three of these parameters are calculated at the point of closest approach of the track with respect to the interaction point, where the two beams collide. In reality, the interaction point is not a point but it is very small extended region that lies close to the center of the detector. However, for simplicity, the interaction point in this study is assumed to be at the center of the detector, i.e. at the origin of the coordinate system.

The five canonical track parameters are,

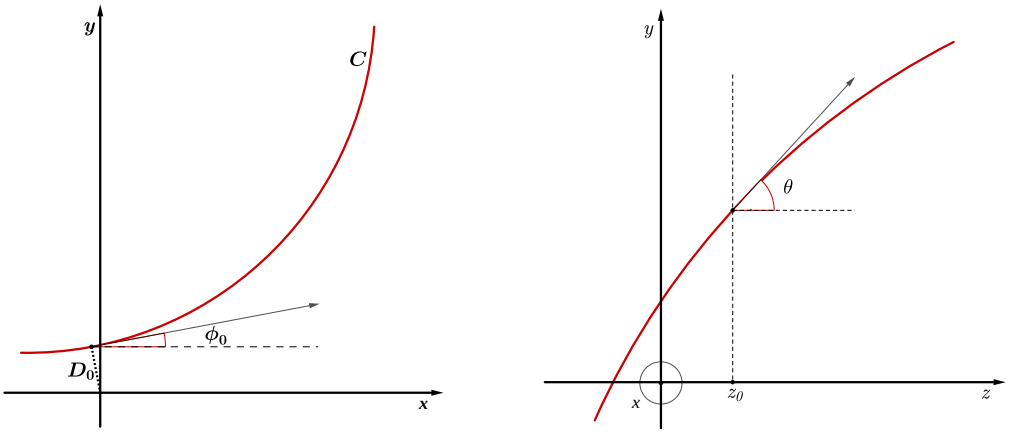

Figure 6.1: Canonical parameters of a particle track. The red curve indicates the trajectory of the particle. $\odot$ sign in the second illustration depicts that the positive x-axis points out of the page.

1. λ is related to the polar angle of the track. $\lambda = \cot(\theta)$, where θ is the polar angle with respect to the $+z$ axis.

2. C defines the curvature of the track through $C = 1/2R$, where R is the radius of curvature of the track. It is a signed parameter; it is positive for negatively-charged particles, and negative for positively charged particles.

3. ϕ_0 is the azimuthal angle of the track momentum at the point of closest approach to the origin.

4. D_0, the signed transverse impact parameter is defined as the distance between the beam pipe and the point of closest approach of the track to the origin in the transverse plane. The sign of the transverse impact parameter is defined indirectly by the sign of the product D_0C; this product is negative if the origin of the coordinate system is located inside the track circle in the transverse plane, and it is positive if the origin is outside the track circle.

5. z_0, the longitudinal impact parameter is the z coordinate of the track at the point of closest approach to the origin in the transverse plane.

The geometrical representation of the five canonical parameters is shown in Figure 6.1.

Another representation, known as W representation, is used for kinematic fitting and for finding momentum at any arbitrary point on the helical trajectory. It consists of the position and momentum evaluated at a particular point.

6.1 Equations of Motion

Assuming a particle having charge Q moving in a magnetic field of magnitude B Tesla, in the direction of the positive z-axis. The particle traverses a helical trajectory with a signed radius of curvature R, being positive for counterclockwise direction of motion. (x, y, z), measured in meters, is an arbitrary point on the helix and (p_x, p_y, p_z, E), measured in GeV, is the 4-momentum of the particle at this point; while (x_0, y_0, z_0) is the known point on the helix, chosen here as the point of closest approach, and $(p_{0x}, p_{0y}, p_{0z}, E_0)$ is the known 4-momentum of the particle at this point. It is useful to define some parameters before presenting the equations of motion:

$$\begin{aligned} p_\perp &= \sqrt{p_x^2 + p_y^2}, \\ a &= -0.2998BQ, \\ \rho &= \frac{1}{R} = 2C = \frac{-0.2889BQ}{p_\perp} \equiv \frac{a}{p_\perp}. \end{aligned} \tag{6.2}$$

The unit of R is meters. The helix trajectory of the charged particle track is then governed by:

$$\begin{aligned} p_x &= p_{0x}\cos(\rho s_\perp) - p_{0y}\sin(\rho s_\perp), \\ p_x &= p_{0y}\cos(\rho s_\perp) + p_{0x}\sin(\rho s_\perp), \\ p_z &= p_{0z}, \qquad E = E_0, \\ x &= x_0 + \frac{p_{0x}}{a}\sin(\rho s_\perp) - \frac{p_{0y}}{a}(1 - \cos(\rho s_\perp)), \\ y &= y_0 + \frac{p_{0y}}{a}\sin(\rho s_\perp) + \frac{p_{0x}}{a}(1 - \cos(\rho s_\perp)), \\ z &= z_0 + \lambda s_\perp \end{aligned} \tag{6.3}$$

These equations are functions of $s_\perp$, which is the arc length between the points (x, y, z) and (x_0, y_0, z_0) in the transverse plane[24].

6.1.1 Track Equations in Cylindrical Coordinates

Sometimes, it is useful to express the track equations in cylindrical coordinates, especially during vertex fitting. In cylindrical coordinates and using the canonical track parameters, the helix can be represented as follows:

$$\begin{aligned} \sin(\phi-\phi_0) &= \frac{rC+(D_0/r)(1+CD_0)}{1+2CD_0} = \frac{D_0}{r}+\frac{(C/r)(r^2-D_0^2)}{1+2CD_0}, \\ \pm\cos(\phi-\phi_0) &= \frac{\sqrt{(1-D_0^2/r^2)[(1+CD_0)^2-r^2C^2]}}{1+2CD_0}, \\ z-z_0 &= \lambda s_\perp, \qquad \sin(Cs_\perp) = C\sqrt{\frac{r^2-D_0^2}{1+2CD_0}}. \end{aligned} \tag{6.4}$$

Here, $r=\sqrt{x^2+y^2}$ and ϕ represent the point on the track in the transverse plane. It should be noted that $\phi-\phi_0=\pi/2$ at the point of closest approach. The sign of $\cos(\phi-\phi_0)$ is positive if the particle is on the outgoing branch of the circle and negative if it is on the incoming branch.

6.2 Track Parameters

The canonical track parameters $(\lambda, C, \phi_0, D_0, z_0)$ can be determined from the instantaneous position (x, y, z) and momentum (p_x, p_y, p_z, E) of the particle at any arbitrary point on the helical trajectory.

$$\begin{aligned} \lambda &= \cot(\theta) = p_z/p_\perp, \\ C &= \rho/2 = a/2p_\perp, \\ \cos(\phi_0) &= \frac{p_x+ay}{T}, \quad \sin(\phi_0) = \frac{p_y-ax}{T}, \\ D_0 &= \frac{1}{a}[T-p_\perp] = \frac{-2(xp_y-yp_x)+a(x^2+y^2)}{T+p_\perp}, \\ z_0 &= z-s_\perp. \end{aligned} \tag{6.5}$$

Here, $T=\sqrt{p_\perp^2-2a(xp_y-yp_x)+a^2(x^2+y^2)}$.

The track parameters have been calculated through these equations in the vertex fitting algorithm used in this study.

6.3 Track Parametrisation

Since the vertex fitting and flavour identification algorithms presented in this thesis uses the canonical track parameters and the covariance matrix of each track, track parametrisation is performed on the tracks after they are simulated. For each particle track, the canonical parameters and a covariance matrix, consisting of the variance of all the five track parameters, can be calculated if a point on the track, its momentum at that point, and its charge are known. All of these three properties are measured in a particle detector. The covariance matrix of the particle tracks depends on the resolution of the particular detector.

6.3.1 Emulating Particle Tracking for IDEA

For any set of track parameters, there will be uncertainties corresponding to the measured track parameters. While using the canonical parameters, these uncertainties are expressed through a 5×5 covariance matrix. These uncertainties arise from two sources, multiple scattering and uncertainties on the point measurements from which the track is reconstructed. To study this for a new detector concept a full simulation of the detector is often employed. The particle is sent through and is tracked step-by-step through the detector, taking into account all possible secondary processes that the particle is expected to undergo; like bremsstrahlung radiation, the hadronic interactions, multiple scattering etc. Then the electronic pulses of the sensitive detector elements are simulated, from which the particle track is reconstructed.

This is computationally very complex. But this process can be emulated, as has been done for the IDEA detector concept by Franco Bedeschi[25], and is used in this study. If the charge, the production vertex and the momentum of a simulated particle is known, it can be calculated how much material this particle would traverse in the detector. The resolution due to multiple scattering can then be estimated if the material distribution is known; as a function of radius for the barrel region and as a function of z for the end-caps. From the trajectory of the particle, it can also be calculated, at which radius the particle would be measured by the sensitive layers inside the tracking detector, from this the expected measurement uncertainty can also be deduced

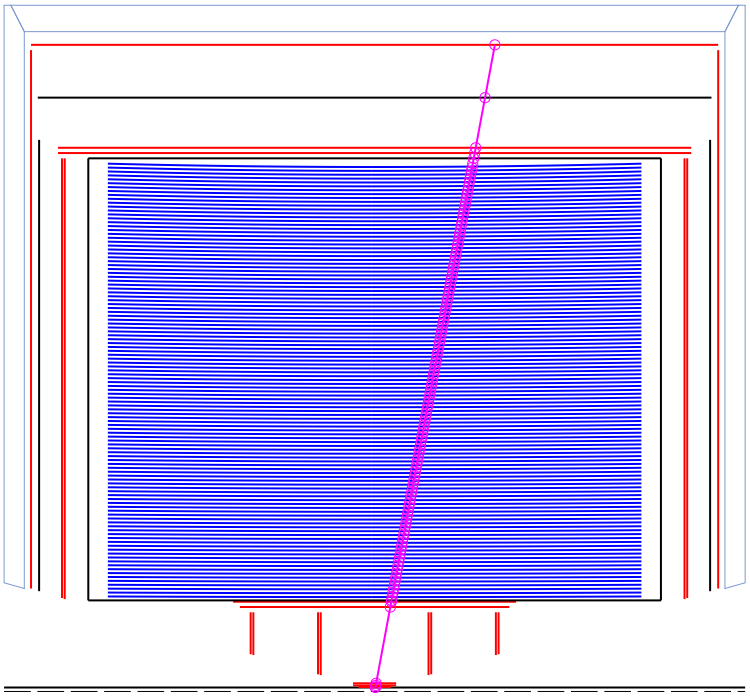

Figure 6.2: The projection of a particle passing through the emulation of the IDEA detector concept in the (y, z)-plane.[25]

based on the point resolution of these measurement layers. Figure 6.2 shows a track passing through the emulated IDEA detector design.

For a simulated "truth" track, a corresponding "observed" track with momentum uncertainty based on the 5×5 covariance matrix is also obtained.

Figure 6.3 shows the measurement uncertainties for the IDEA drift chamber compared to those for the state-of-the-art tracking detector of CLD, based only on silicon sensors. Because of the extremely light drift chamber of the IDEA detector concept, it has a considerably smaller uncertainty due to multiple scattering, as represented by the dashed lines in the upper-left plot of Figure 6.3. Though the CLD tracking detector has a better detector resolution, as signified by the lower slop of the red solid line in the upper-left plot of Figure 6.3, the final tracking resolution is better for the IDEA drift chamber in the momentum range of interest. Since the beam pipe radius of FCC-ee is small, the possible impact parameter resolution can be as small as 3-5 μm, which for the purpose of flavour identification is very advantageous.

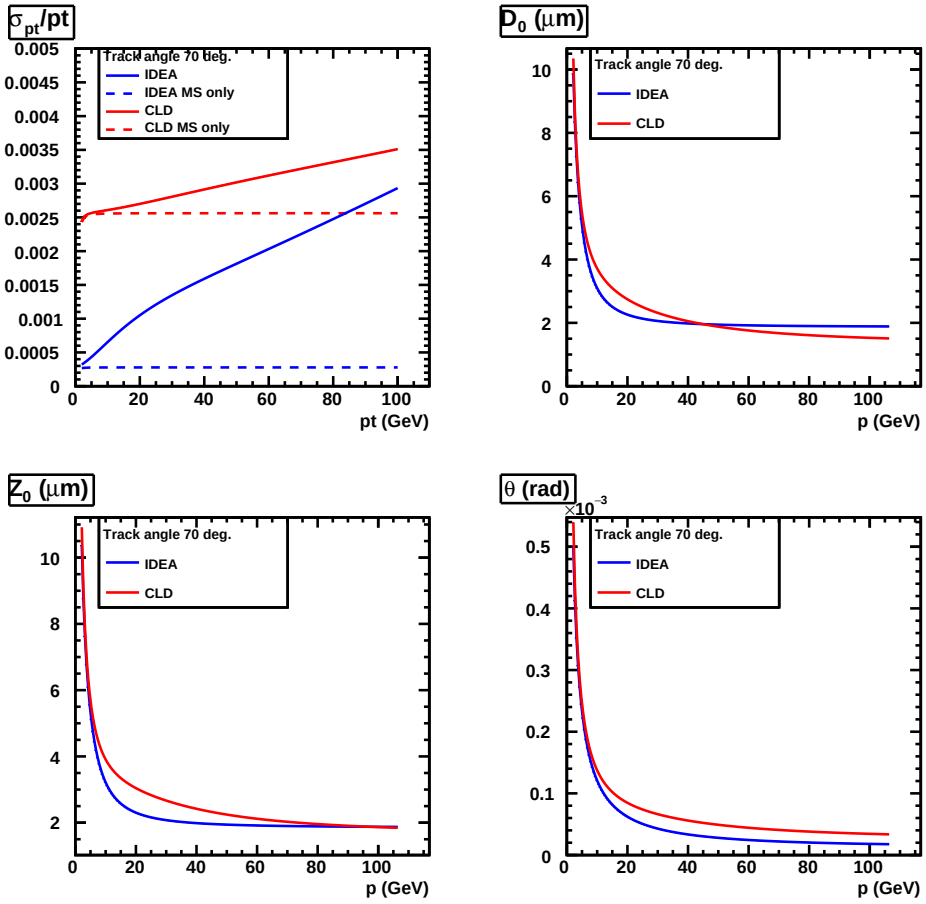

Figure 6.3: Measurement uncertainties as a function of particle momentum for a particle track with polar angle 70° being observed in IDEA and CLD detector concepts. The upper-left plot shows the uncertainties on the momentum measurements as a function of the transverse momentum; MS stands for multiple scattering. The upper-right and the lower-left plots show the uncertainties on the transverse and longitudinal impact parameter measurements. The lower-right plot shows the uncertainties on the polar angle measurements.[25]

7 Vertex Fitting

Fitting particle tracks to the corresponding decay vertices, where they originate from, is an integral part of event reconstruction. A vertex fitting algorithm takes as input a set of charged particle tracks and finds a point in three-dimensional space where these tracks are likely to have originated from.

The following algorithm[25] uses the track parameters of a given set of tracks and varies them, with the deviations controlled by their covariance matrix to fit the set of tracks to a common vertex.

7.1 Algorithm

The vertex fitting algorithm proceeds in the following way:

- The canonical track parameters of all the tracks and a preliminary estimate for the vertex position are taken as the initial points for the fit.
- The track parameters are updated to make all the tracks pass through a common vertex point keeping the χ^2 value to a minimum.
  - The χ^2 for the fit is subjected by constraints corresponding to the longitudinal and transverse projections of the particle track.

- A deviation from the preliminary estimate is calculated depending on the updated track parameters, giving the common vertex position.

7.2 Analysis

A set of N tracks with track parameters $\vec{\alpha}_i$, which are 5- dimensional vectors representing the five canonical track parameters, and covariance matrices C_i can be fitted to a vertex by letting the track parameters float so that all tracks can meet at a common point $\vec{x}$, which is a 3- dimensional position vector. The possible track variations are controlled by their corresponding covariance matrix. To fit the tracks to a common vertex point using this technique, the χ^2,

$$\chi^2 = \sum_{i=1}^{N} (\vec{\alpha}_i - \vec{\alpha}_i^0)^t C_i^{-1} (\vec{\alpha}_i - \vec{\alpha}_i^0) = \sum_{i=1}^{N} \delta\vec{\alpha}_i^t C_i^{-1} \delta\vec{\alpha}_i, \tag{7.1}$$

has to be minimised subject to two constraint equations for each track, which correspond to the longitudinal and transverse track projections, given by Equation 7.16. Here $\vec{\alpha}_i^0$ represents the initial track parameters. These constraints can be expressed in vector form as,

$$\vec{f}_i(\vec{\alpha}_i, \vec{x}) = 0. \tag{7.2}$$

The above problem of minimising the χ^2 subjected to the given constraints can be reformulated by introducing a set of $2N$ Lagrange multipliers, $\vec{\lambda}_i$, to that of minimising the modified χ^2,

$$S = \chi^2 + 2\sum_{i=1}^{N} \vec{\lambda}_i^t \vec{f}_i(\vec{\alpha}_i, \vec{x}). \tag{7.3}$$

$\vec{\alpha}_i^0$ and a guess of the common vertex point, $\vec{x}^0$, can now be used as the starting points for a first-order expansion of the constraints,

$$\vec{f}_i = \vec{f}_i(\vec{\alpha}_i^0, \vec{x}^0) + \frac{\partial \vec{f}_i}{\partial \vec{\alpha}_i}(\vec{\alpha}_i - \vec{\alpha}_i^0) + \frac{\partial \vec{f}_i}{\partial \vec{x}_i}(\vec{x} - \vec{x}_0) = \vec{f}_i^0 + D_i \delta\vec{\alpha} + B_i \delta\vec{x} \tag{7.4}$$

The matrices D_i and B_i have been defined here as the partial derivatives of the constraint vector with respect to the canonical track parameters and the vertex position respectively. Their mathematical form is derived in Section 7.2.1. This first-order expansion is then inserted in the definition of S and the minimising

problem is solved by setting all derivatives of S, with respect to $\vec{\alpha}_i$, $\vec{x}$, and $\vec{\lambda}_i$, equal to zero. This produces the following system of linear equations,

$$\frac{1}{2}\frac{\partial S}{\partial \vec{\alpha}_i} = C_i^{-1}\delta\vec{\alpha}_i + D_i^t\vec{\lambda}_i = 0, \tag{7.5}$$

$$\frac{1}{2}\frac{\partial S}{\partial \vec{\lambda}_i} = \vec{f}_i^0 + D_i\delta\vec{\alpha}_i + B_i\delta\vec{x} = 0, \tag{7.6}$$

$$\frac{1}{2}\frac{\partial S}{\partial \vec{x}} = \sum_i B_i^t\vec{\lambda}_i = 0, \tag{7.7}$$

Using the first of this system of equations, $\delta\vec{\alpha}_i$ can be expressed in terms of $\vec{\lambda}_i$. This can be used to replace $\delta\vec{\alpha}_i$ in the second equation to find $\vec{\lambda}_i$ as a function of $\vec{x}$. This, when put in the third equation, produces an equation with $\vec{x}$ as the only variable. It can then be solved to return,

$$\delta\vec{x} = -H\sum_{i=1}^{N}(B_i^t W_i \vec{f}_i^0). \tag{7.8}$$

Here, the two newly introduced matrices are defined as,

$$W_i = (D_i C_i D_i^t)^{-1}, \tag{7.9}$$

$$H = (\sum_i B_i^t W_i B_i)^{-1}. \tag{7.10}$$

H is the covariance matrix of the vertex position vector $\vec{x}$. The other unknown parameters can also be expressed in the same notation using Equation 7.8,

$$\vec{\lambda}_i = W_i(\vec{f}_i^0 + B_i\delta\vec{x}), \tag{7.11}$$

$$\delta\vec{\alpha}_i = -C_i D_i^t W_i(\vec{f}_i^0 + B_i\delta\vec{x}). \tag{7.12}$$

And the χ^2 can then be expressed as,

$$\begin{aligned}\chi^2 &= \sum_{i=1}^{N}\delta\vec{\alpha}_i^t C_i^{-1}\delta\vec{\alpha}_i, \\ &= \sum_{i=1}^{N}(\vec{f}_i^{0t} + \delta\vec{x}^t B_i^t)W_i D_i C_i C_i^{-1} C_i D_i^t W_i(\vec{f}_i^0 + B_i\delta\vec{x}), \\ &= \sum_{i=1}^{N}\vec{\lambda}_i^t W_i^{-1}\vec{\lambda}_i. \end{aligned} \tag{7.13}$$

Thus $\delta\vec{x}$ gives the deviation from the initial guess and $\delta\vec{\alpha}_i$ gives the deviation from the initial track parameters to obtain the vertex position $\vec{x}$.

7.2.1 Constraints and Derivatives

The mathematical form of the constraints, defined in Equation 7.2, and their derivatives with respect to the track parameters and the vertex coordinates, respectively, defined in Equation 7.4 are derived from the track equations Equation 6.4.

If $\vec{x} = (x, y, z)$ is a point on the track, we can replace the cylindrical coordinates (r, ϕ, z) with these Cartesian coordinates (x, y, z). This transforms Equation 6.4 in the following manner,

$$r\sin(\phi - \phi_0) = y\cos(\phi_0) - x\sin(\phi_0) = \frac{r^2C + (1 + CD_0)D_0}{1 + 2CD_0}, \tag{7.14}$$

$$\sin^2(C\frac{z - z_0}{\lambda}) = C^2\frac{(r^2 - D_0^2)}{(1 + 2CD_0)}. \tag{7.15}$$

Here, $r^2 = x^2 + y^2$.

Since the vertex position should be on the particle track, this provides two constraints that track parameters are subjected to while fitting them to a common vertex. As the constraints were expressed in the form of a vector in the formalism presented in the previous section, the two components of this vector are given by,

$$f_1(\vec{\alpha}, \vec{x}) = \frac{r^2C + (1 + CD_0)D_0}{1 + 2CD_0} - y\cos(\phi_0) + x\sin(\phi_0) = 0, \tag{7.16}$$

$$f_2(\vec{\alpha}, \vec{x}) = \sin^2(C\frac{z - z_0}{\lambda}) - C^2\frac{(r^2 - D_0^2)}{(1 + 2CD_0)} = 0. \tag{7.17}$$

The matrices D and B have been defined as the derivatives of the constraint vector $\vec{f}(\vec{\alpha}, \vec{x})$. Therefore they can be calculated from the above equations. The derivative with respect to the track parameters considers the order of track parameters as $(D_0, \phi_0, C, z_0, \lambda)$.

$$D = \frac{\partial \vec{f}}{\partial \vec{\alpha}} = \begin{pmatrix} 1 - \frac{2C(D_0 + C(r^2 - D_0^2))}{(1+2CD_0)^2} & x\cos(\phi_0) + y\sin(\phi_0) & \frac{r^2 - D_0^2}{(1+2CD_0)^2} & 0 & 0 \\ \frac{2C^2(Cr^2 + D_0(1+CD_0))}{(1+2CD_0)^2} & 0 & \frac{z-z_0}{\lambda}\sin(C\frac{z-z_0}{\lambda}) & \frac{C}{\lambda}\sin(C\frac{z-z_0}{\lambda}) & C\frac{z-z_0}{\lambda^2}\sin(C\frac{z-z_0}{\lambda}) \end{pmatrix} \tag{7.18}$$

Similarly:

$$B = \frac{\partial \vec{f}}{\partial \vec{x}} = \begin{pmatrix} \frac{2Cx}{1+2CD_0} + \sin(\phi_0) & \frac{2Cy}{1+2CD_0} - \cos(\phi_0) & 0 \\ \frac{-2xC^2}{1+2CD_0} & \frac{-2yC^2}{1+2CD_0} & \frac{C}{\lambda}\frac{z-z_0}{\lambda} \end{pmatrix} \tag{7.19}$$

The matrices W and H and the Lagrangian multipliers can be calculated from $\vec{f}$, D, and B using Equation 7.9 and Equation 7.11.

7.3 Preliminary Vertex Estimate

As stated previously, a guess for the vertex position is required to initialise the vertex fitting algorithm. It is often useful to have a preliminary estimate to initialise the vertex fit. One straightforward way to do this relies on mapping tracks onto points and vertices onto tracks.

Considering a set of tracks originating from the same vertex, the position of which is given by $\vec{x}_V = (x_V, y_V, z_V)$, the track equation for all these tracks at the vertex point can be described as,

$$\phi_V = \phi(r_V) = \phi_{0,i} + \sin^{-1}\left(\frac{r_V C_i + (1 + C_i D_{0,i}) D_{0,i}/r_V}{1 + 2C_i D_{0,i}}\right), \tag{7.20}$$

$$z_V = z(r_V) = z_{0,i} + \frac{\lambda_i}{C_i}\sin^{-1}\left(C_i\sqrt{\frac{rV^2 - D_{0,i}^2}{1 + 2C_i D_{0,i}}}\right). \tag{7.21}$$

Here $r_V = \sqrt{x_V^2 + y_V^2}$, and the index i identifies the individual tracks.

The track equation in the transverse plane can be rewritten in a similar way as shown in the previous section,

$$\begin{aligned} r_V \sin(\phi_V - \phi_{0,i}) &= y_V \cos(\phi_{0,i}) - x_V \sin(\phi_{0,i}) \\ &= \frac{r_V^2 C_i + (1 + C_i D_{0,i}) D_{0,i}}{1 + 2C_i D_{0,i}} = D_i' \approx D_{0,i}. \end{aligned} \tag{7.22}$$

The approximation in the last step assumes that $C_i D_{0,i}$, $C_i r_V \ll 1$, which is generally the case. This suggests that the transverse vertex position can be fitted by minimising the following χ^2,

$$\chi^2 = \sum_{i=1}^{N} \frac{(\vec{n}_i^t x_V - D_{0,i})^2}{\sigma^2_{D_0,i}} \tag{7.23}$$

with $\vec{n}_i = (-\sin(\phi_{o,i}), \cos(\phi_{0,i}))$. This results in the transverse position vector,

$$\vec{x}_V = \left(\sum_{i=1}^{N} \frac{\vec{n}_i \vec{n}_i^t}{\sigma^2_{D_0,i}} \right)^{-1} \left(\sum_{i=1}^{N} \frac{D_{0,i} \vec{n}_i^t}{\sigma^2_{D_0,i}} \right) \tag{7.24}$$

and the covariance matrix,

$$\text{Cov}(\vec{x}_V) = \left(\sum_{i=1}^{N} \frac{\vec{n}_i \vec{n}_i^t}{\sigma^2_{D_0,i}} \right)^{-1}. \tag{7.25}$$

This estimate can be refined by iterating this fit and using the corrected impact parameter,

$$D_i' = \frac{r_V^2 C_i}{1 + 2C_i D_{0,i}} + \frac{1 + C_i D_{0,i}}{1 + 2C_i D_{0,i}} D_{0,i}. \tag{7.26}$$

This corrected impact parameter can then be recalculated using the previous estimate of r_V.

For the same approximation, $C_i r_V \ll 1$, the longitudinal track equation can be simplified to,

$$\begin{aligned} z_V = z(r_V) &= z_{0,i} + \frac{\lambda_i}{C_i} \sin^{-1}\left(C_i \sqrt{\frac{r_V^2 - D_{0,i}^2}{1 + 2C_i D_{0,i}}} \right) \\ &\approx z_{0,i} + \lambda_i \sqrt{\frac{r_V^2 - D_{0,i}^2}{1 + 2C_i D_{0,i}}} = z_{0,i} + \lambda_i R_i'. \end{aligned} \tag{7.27}$$

Thus the longitudinal vertex position can be obtained by using the r_V found from the transverse fit and minimising the following χ^2,

$$\chi^2 = \sum_{i=1}^{N} \frac{(z_V - z_{0,i} - \lambda_i R_i')^2}{\sigma^2_{z_0,i}}. \tag{7.28}$$

that results in,

$$z_V = \frac{\sum_i (z_{0,i} + \lambda_i R_i')/\sigma^2_{z_0,i}}{\sum_i 1/\sigma^2_{z_0,i}}. \tag{7.29}$$

This estimate $\vec{x}_V = (x_V, y_V, z_V)$ can then be used to initialise the vertex fitting algorithm.

7.4 Performance Review

To report the performance of the vertex fitting algorithm, a few experimental scenarios are introduced, where artificially generated tracks are fitted to a common vertex.

To generate a track, first, a flight distance and a direction have to be chosen for the decay vertex, where the track originated from. The range for the polar angle is kept from 40° to 140°, which is also referred to as the barrel region. A value is chosen at random for the polar angle of the decay vertex position. The azimuthal angle, between 0° to 360°, for the decay vertex position is also chosen randomly. Similarly, the flight distance is chosen at random from a range, which can be selected to be different for different cases. The Cartesian coordinates of the decay vertex are then calculated from the flight distance, the polar angle, and the azimuthal angle.

Multiple tracks can be generated from each individual decay vertex. A momentum magnitude, between 1 GeV and 20 GeV, is randomly chosen for each of these tracks. To get the direction of the momentum, the polar angle is chosen from a Gaussian distribution with a mean as the polar angle of the decay vertex position and a width of 0.10 radians. The azimuthal angle is chosen in a similar way but with the width of the Gaussian distribution being 0.20 radians. Using the magnitude and the two angles, the x, y, and z projections of the momentum of the track are calculated. The charge is also chosen at random, with it being positive half of the time and negative the other half.

Once a track is generated, it is passed through the track parametrisation routine, which calculates the canonical track parameters and the covariance matrix, and gives the "observed" track. Figure 6.3 shows that the detector design used provides a very good momentum and angular resolutions.

To test the performance of the vertex fitting algorithm, first tracks originating from a common decay vertex were fitted to a vertex. In each event, four

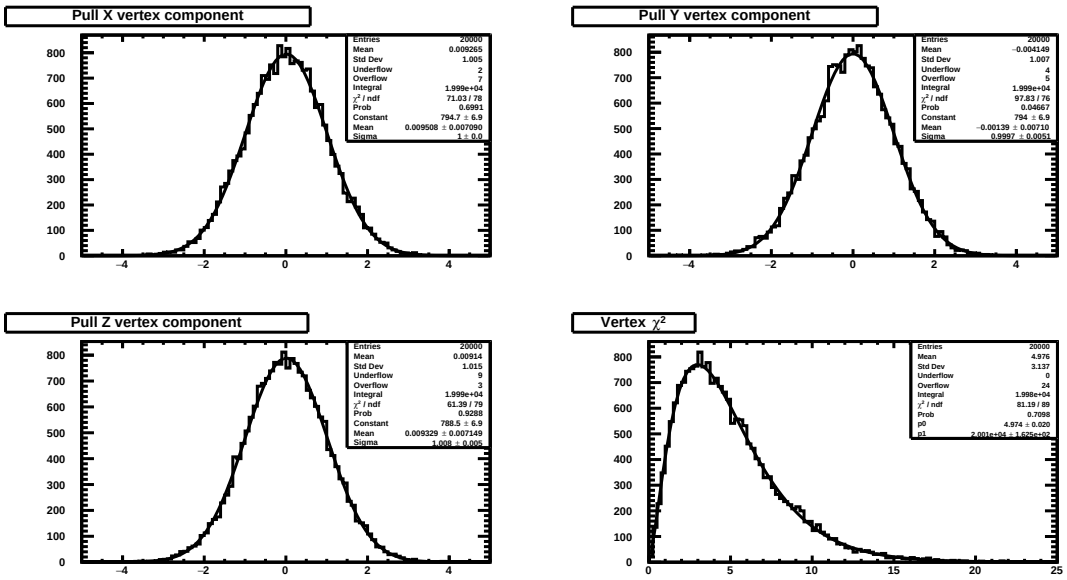

Figure 7.1: The pull on the three vertex position coordinates and the corresponding χ^2 value after performing vertex fitting on events with four tracks originating from a common production vertex. The pull on the vertex coordinates are plotted with a Gaussian fit and the χ^2 values are plotted with a χ^2 fit with five degrees of freedom.

tracks were generated from a decay vertex. 20000 such events were simulated with the flight distance of the decay vertex ranging from 1 mm to 5 mm. The resolutions of the three vertex position components after performing the vertex fit are shown in Figure 7.1. The pull on the x-coordinate in the figure is defined by,

$$\text{pull}(x) = \frac{x_V - x_P}{\sigma_{x_V}}. \tag{7.30}$$

Here, x_V is the x-coordinate of the reconstructed vertex and x_P is the x-coordinate of the production vertex, and σ_{x_V} is the uncertainty in the measurement of the x-coordinate of the reconstructed vertex position. The pull on the y- and z-coordinates is defined in the same way. Figure 7.1 also shows the distribution of the χ^2 values obtained while fitting all the vertices individually.

In a second scenario, in each event, three tracks were generated from a common decay vertex and one track was generated from a different decay vertex with a randomly chosen flight distance within the same range of 1-5 mm. All four tracks from each event were forced to fit to a common vertex. The resolution of the three vertex position components for these fits are shown in Figure 7.2. The change in the scale of the x-axis for the distributions showing

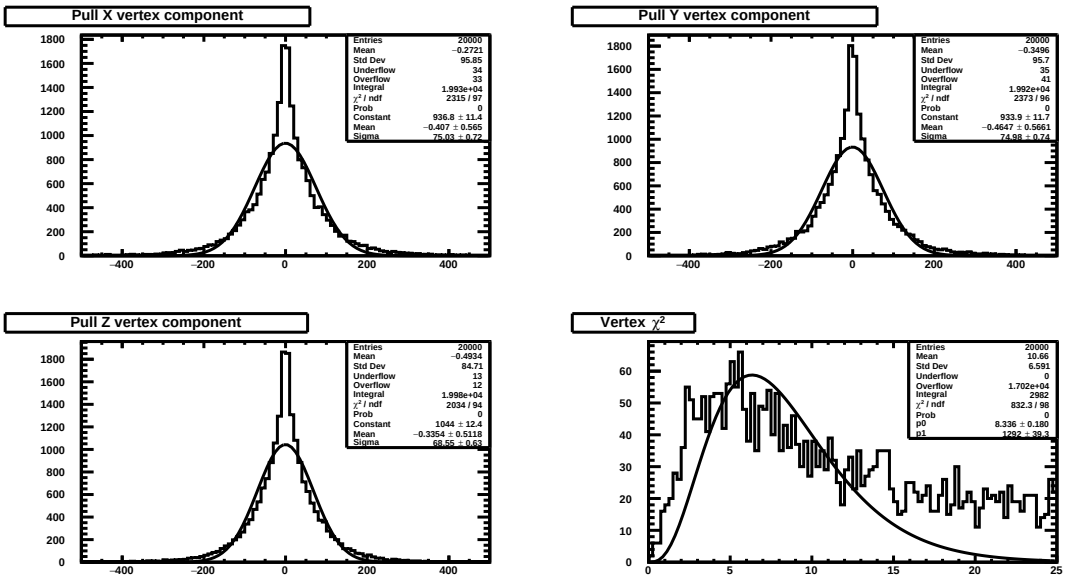

Figure 7.2: The pull on the three vertex position coordinates and the corresponding χ^2 value after performing vertex fitting on events with three tracks originating from a common production vertex and one track originating from a different production vertex. The pull on the vertex coordinates are plotted with a Gaussian fit and the χ^2 values are plotted with a χ^2 fit with five degrees of freedom.

the spatial resolutions should be noted. As can be seen that the χ^2 values corresponding to these fits are significantly larger than those for the previous scenario and only 15% events are inside the window shown in the plots. This test depicts that a reliable χ^2 fit, along with other necessary constraints, can be performed on the vertices obtained from this fitting algorithm to separate tracks originating from different decay vertices, since when a track originating from a different decay vertex is fitted to a vertex with a set of tracks originating from a common decay vertex, then the algorithm returns a large χ^2 value. A threshold can thus be set on the χ^2 values to choose vertices with a reasonable χ^2 value.

The vertex fitting algorithm explored in this chapter is an integral part of the flavour identification methods presented later. The two scenarios described above show that the χ^2 value is very sensitive to the set of tracks being passed through the vertex fit. This is essential to achieve good performance while separating tracks originating from different decay vertices. Further in the thesis, wherever it is stated that a vertex fit has been performed, it is implied that this algorithm has been implemented for the purpose.

8 A Common Process for Performance Review

Before presenting the flavour identification algorithms, it is beneficial to report a benchmark process that has been used to study and analyse the performance of all of these algorithms. The hadronic decays of the Z boson produced at the Z-pole in the e^+e^- collisions is the process used in this thesis. Apart from being a well understood process, it is also one of the targets of the study at FCC-ee, where about 5×10^{12} Z bosons are projected to be produced. For high-precision measurements of the branching fractions of the decay channels $Z \to b\bar{b}, c\bar{c}$, identifying the flavour of these events is important; and since the objective of this thesis is to present techniques for flavour identification to distinguish between these different hadronic decay modes, the events with the Z boson decaying to a quark-antiquark pair are simulated; separately to bottom, charm, and light quark-antiquark pairs. These are also the dominant decay modes, as can be seen in Table 8.1. Hence the process can be represented as,

$$e^+e^- \to \gamma^*/Z \to q\bar{q}. \tag{8.1}$$

Figure 8.1 shows the Feynman diagram for this production process.

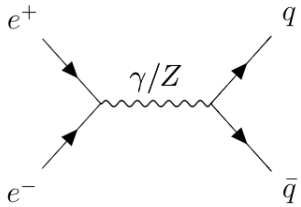

Figure 8.1: The Feynman diagram for the process introduced in Equation 8.1.

Decay Mode	Branching Ratio
hadrons	$\approx 69.9\%$
up-type quarks	$\approx 11.6\%$
down-type quarks	$\approx 15.6\%$
$\ell^+\ell^-$	$\approx 10\%$
$\nu\bar{\nu}$	$\approx 20\%$

Table 8.1: Branching ratios of major decay modes of Z boson.[1]

This process is studied by simulating electron-positron collisions in Pythia[26] [27] at the center-of-mass energy of 91.1876 GeV to produce Z bosons using the process - `WeakSingleBoson:ffbar2gmZ`. The events where the Z boson decays to a bottom quark-antiquark pair have been referred to as bottom flavoured events. Charm and light flavoured events are defined in the same fashion.

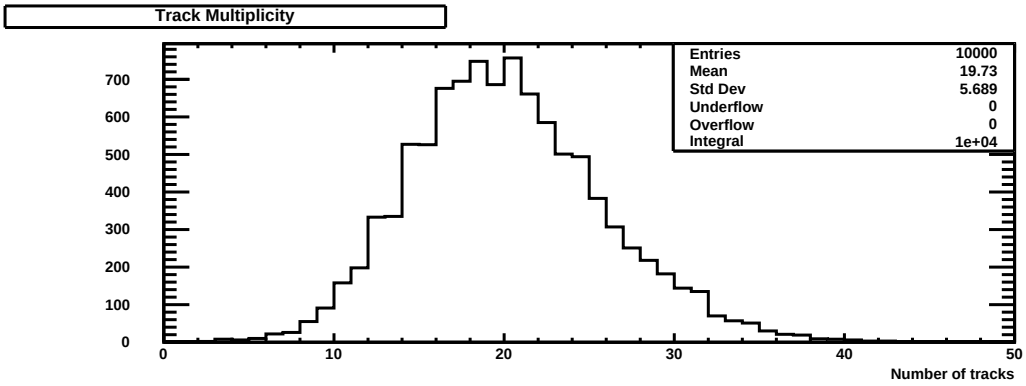

Figure 8.2: The charged track multiplicity after applying the selection criteria on $10{,}000$ $Z \to b\bar{b}$ events.

Since the track parametrisation has been done in this study by emulating the IDEA detector design, therefore the particle track selection has been performed accordingly. The charged final particle tracks produced in the event are stored. To limit the particle tracks inside the angular range of the IDEA detector, all the tracks which have a cosine of the polar angle greater than 0.975 were excluded. All the soft particle tracks, i.e. the tracks with small momentum magnitudes, are also discarded. The threshold on momentum magnitude was kept at 300 MeV. The track multiplicity after applying the selection is shown in Figure 8.2.

8.1 Jet Clustering

Due to hadronisation, hadronic decay events are observed in the form of jets of hadronic particles in a detector. Reconstructing these jets from the observed particle tracks makes it easier to study the event and identify the hadron that produced them. This process is called jet finding or jet clustering. It is an essential step in all flavour identification algorithms illustrated in this thesis.

In this study, jet clustering has been performed using `ee-kt algorithm`, sometimes referred to as $Durham\ algorithm$, in FastJet[28]. It involves a distance measure between two particles, d_{ij}, for all pairs of particles,

$$d_{ij} = 2\min(E_i^2, E_j^2)(1 - \cos\theta_{ij}), \tag{8.2}$$

where E_i is the energy of the i'th particle and θ_{ij} is the opening angle between the i'th and j'th particles at their production point. If d_{ij} is smaller than a threshold value d_{cut}, then the two particles are replaced with a single new object, often called a pseudo-jet, with a momentum $p = p_i + p_j$. This is repeated until the smallest d_{ij} is above the threshold. The resulting pseudo-jets or particles are the jets of the event. The required number of jets can be specified by the user; in such cases the threshold value is calculated dynamically to satisfy this requirement. This way, the events generated for this study are forced into two jets.

9 Invariant Mass

The invariant mass is a property of an object or a set of objects that is independent of the Lorentz frame or the frame of reference of the observer. For a set of objects with energies E_i and momenta $\vec{p}_i = (p_{xi}, p_{yi}, p_{zi})$ it is defined as,

$$\begin{aligned} m &= \sqrt{\left(\sum_i E_i\right)^2 - \left(\sum_i \vec{p}_i\right)^2}, \\ &= \sqrt{\left(\sum_i E_i\right)^2 - \left(\sum_i p_{xi}\right)^2 - \left(\sum_i p_{yi}\right)^2 - \left(\sum_i p_{zi}\right)^2}. \end{aligned} \tag{9.1}$$

To determine the mass of an individual particle in a detector experiment, particle identification has to be performed. But in this study, only the information obtained from the tracking detector is exploited, using which identifying the particles is not possible. Therefore, the mass of pions is used to calculate the expected energy of the particles, except while searching for Λ^0 and photon conversion vertices (Chapter 11). This energy, along with the "observed" momentum has been used to calculate the invariant mass of particles with Equation 9.1.

The vertex fitting routine used in this study to find reconstructed vertices does not return the updated track parameters of the "observed" tracks after the fit has been performed. Therefore, the momentum of the "observed" particles at the point closest to the vertex point has to be calculated from the known momentum of the particles at the point of closest approach to measure the invariant mass of the vertex, which is the invariant mass of the set of tracks

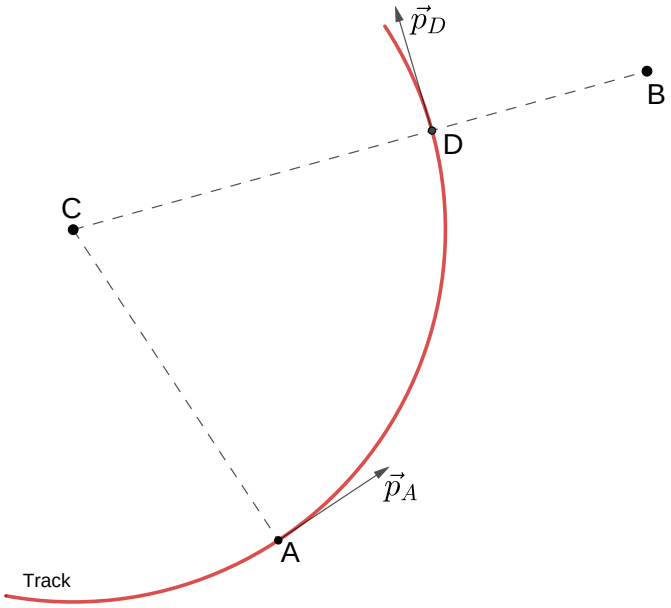

Figure 9.1: Particle track in the (x, y)-plane. $\vec{p}_A$ and $\vec{p}_D$ are the momentum vectors of the particle at points A and D respectively. The points have been defined in Section 9.1.

forming the vertex. The following analysis shows the procedure, which has been used to propagate the momentum.

9.1 Mathematical Analysis

Figure 9.1 shows the projection of a track in the (x, y)-plane, therefore the momentum and the position vectors are the transverse projections of the complete vectors. The point C represents the center of the circle of the particle track. This track, along with other tracks has been fitted to a vertex, which is represented by point B. Point D represents the point of closest approach to the vertex at B. Point A represents the point, where the momentum and the coordinates of the track are known. To calculate the momentum of the track at the point D from the known information at point A and point B is done in the following way.

$$\vec{r}_C = \vec{r}_A + \frac{\hat{p}_A}{a} \tag{9.2}$$

Here, $\vec{r}_i$ is a radial vector from the origin to the point i; $\hat{x}$ is the vector obtained by rotating a vector $\vec{x}$ by $+\frac{\pi}{2}$ radians; and a is the variable defined in Equation 6.2. Then the displacement vector from C to B can be defined as,

$$\begin{aligned}\vec{r}_{CB} &= \vec{r}_B - \vec{r}_C = \vec{r}_B - \vec{r}_A - \frac{\hat{p}_A}{a} \\ &= \vec{r}_{AB} - \frac{\hat{p}_A}{a}\end{aligned} \tag{9.3}$$

The magnitude of this vector, $r_{CB} = |\vec{r}_{CB}|$, can be calculated using Equation 9.3. Since, the magnitude of the momentum of the particle at point D would be the same as that at point A, the momentum vector at the point D can be written as,

$$\vec{p}_D = p\frac{\hat{r}_{CB}}{r_{CB}} = \frac{p}{r_{CB}}(\hat{r}_{AB} + \frac{\vec{p}_A}{a}). \tag{9.4}$$

Here, $p = |\vec{p}_A| = |\vec{p}_D|$, is the magnitude of the track momentum. It should be noted that rotating a vector by $+\frac{\pi}{2}$ radians twice results in the vector in the opposite to the original direction, i.e. $\hat{\hat{x}}$ is $-\vec{x}$.

9.2 Performance Review

One of the most important use of knowing the invariant mass of a vertex is to identify V^0 vertices, which are the decay vertices of neutral particles, like K^0_S that decay into a pair of charged particles. A detailed description of the V^0 vertices is provided in Chapter 11.

Therefore to report the performance of this method of calculating the invariant mass of vertices, $Z \to q'\bar{q}'$ events, with $q' \equiv (u, d, s)$, were generated using the process detailed in Chapter 8 and only the particles that originated from K^0_S decay vertices were selected and the rest of the particles were discarded. Track parametrisation was performed on all of these tracks to calculate their track parameters and the momenta observed at the point of closest approach.

Among these tracks, all possible pairs were fitted to find the two-track vertex candidates for K^0_S vertices. The invariant masses of these vertices were then calculated both before and after propagating the momentum; i.e. once the invariant masses were calculated using the momenta at the point of closest approach and the next time they were calculated at the two-track vertex point

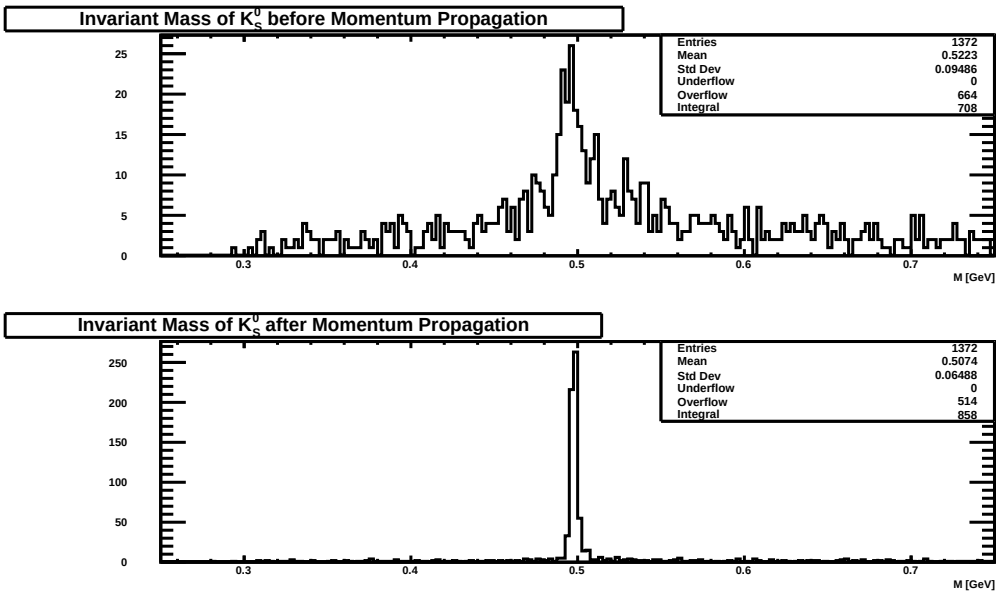

Figure 9.2: Invariant Mass distribution of K^0_S vertex candidates in $Z \to q'\bar{q}'$ events, with $q' \equiv (u, d, s)$, before and after propagating the momentum vector of the particles to the vertex point.

is situated. Figure 9.2 shows the distribution of the invariant masses of the K^0_S candidate vertices for the two scenarios.

As can be seen in Figure 9.2, after using the correct momentum after propagating the momentum vector to the vertex point the peak stands out very clearly in the invariant mass distribution of the K^0_S.

The invariant mass of vertices has been calculated using this procedure throughout this study.

10 Flavour Identification

Decay events to different hadronic flavours are expected to leave distinguishing signatures in the tracking detector, resulting from the distinguishing properties of the hadrons containing different flavours of quarks. In a high-energy particle collision like e^+e^- collisions at the LEP or pp collisions at the LHC, the incoming particles are made to collide inside the detector at a point, which is referred to as the interaction point. The particle collision produces new massive particles, like the weak bosons, the Higgs boson, top quark-antiquark pair etc. depending on the center-of-mass energy, as the incoming particles interact, via the electro-weak interaction in e^+e^- collisions and mainly via the strong interaction in pp collision. These massive particles have negligible lifetimes and they essentially decay at the Interaction Point and produce several particles. This decay vertex is known as the primary vertex. Some of the particles produced at the primary vertex, like bottom and charm hadrons, have small yet finite lifetimes, as can be seen in Table 10.1. These particles travel away from the primary vertex before decaying weakly and such decay vertices are called secondary vertices. In particular the lifetimes of the strange flavoured hadrons are much longer than those of bottom and charm flavoured hadrons.

The secondary vertices in different flavoured hadronic decay events are expected to have different properties. The study presented in this thesis attempt to exploit such properties to accurately identify the flavour of the bottom and charm flavoured hadronic decay events.

Quark	Hadron	Lifetime ($\times 10^{-12}$ s)	Decay Length (mm)	Mass (GeV)
b	B^0	1.5	0.45	5.28
	B^+	1.6	0.48	5.28
	Λ_b^0	1.5	0.45	5.62
c	D^0	0.4	0.12	1.86
	D^+	1.0	0.30	1.87
	Λ_c^+	0.2	0.06	2.29
s	K_S^0	89.5	26.85	0.50
	Λ^0	263.2	78.96	1.12

Table 10.1: Lifetime, decay length, and mass of a few most commonly observed hadrons containing bottom, charm, or strange quarks [1]. The decay length is defined as $c\tau$, where c is the speed of light and τ is the lifetime of the particle in seconds.

The weak decays of the quarks proceed via the charged current weak interaction, and the decay chain in cascading decays of heavy quarks is expected to be,

$$b \to c \to s \to d.$$

This is because the CKM matrix is near-diagonal. Thus a bottom hadron decay chain is expected to have more secondary vertices than a charm or a light hadron decay chain. So the multiplicity of the secondary vertices, reconstructed by fitting charged tracks, found in the jets of the events under consideration may be a useful property to separate the heavy flavoured hadronic decay events from the light flavoured hadronic decay events. This possibility will be explored in Chapter 14. Since the masses of the hadrons containing different quarks is also different, the invariant mass of the secondary vertices should also be different for different flavoured hadronic decay events. The tracks originating from the decay vertices of bottom hadrons should have higher momenta transverse to their jet axes, owing to the higher masses of bottom hadrons. The characteristic flight length or the decay length of bottom hadrons is about 400 μm and that of the charm hadrons is about 80 μm, and as a result, the spatial distribution of the secondary vertices in the bottom and the charm flavoured events may also be different.

A framework, LCFIPlus[29], has been developed within the Linear Collider Collaboration to use these properties for hadronic flavour identification. The jets are categorised according to the secondary vertex multiplicity and then a multivariate analysis is employed using other properties, like mentioned above,

to optimise the separation. The study presented in Chapter 14 is inspired by this framework.

Chapter 12 presents an algorithm to identify the flavour of the hadronic decay events without reconstructing secondary vertices. The impact parameter of tracks originating from the decays of different flavoured hadrons are expected to be different as a result of different lifetimes and masses of these hadrons. Chapter 12 attempts to exploit this property to separate the hadronic decay events.

11 V^0 Particles

V^0 particles are neutral particles that decay or convert into a pair of charged particles. The V^0 decays vertices may have signatures resembling those of bottom or charm hadron decays vertices. Therefore it is necessary to reconstruct and remove these V^0 particles to avoid misidentification of $Z \to s\bar{s}$ events as $Z \to b\bar{b}$ or $Z \to c\bar{c}$ events. This procedure of rejecting the tracks originating from the decays of V^0 particles is referred to as V^0 rejection and is a crucial step during accurately reconstructing secondary vertices, as defined in Chapter 10, formed by bottom and charm hadronic decays.

Dedicated filters are applied for this purpose. The three processes through which the V^0 particles decay or convert are the K^0_S and Λ^0 decays and photon conversions,

$$\begin{aligned} K^0_S &\to \pi^+\pi^- \\ \Lambda^0 &\to p\pi^- \quad \text{OR} \quad \bar{p}\pi^+ \\ \gamma_{conv}X &\to e^+e^-X \end{aligned} \tag{11.1}$$

The V^0 rejection is not performed on all of the tracks from an event but only on the set of tracks, which are expected to have originated away from the interaction point.

	K^0_s		Λ^0		γ_{conv}	
	tight	loose	tight	loose	tight	loose
Mass (GeV)	[0.492, 0.503]	[0.491, 0.504]	[1.113, 1.118]	[1.110, 1.121]	<0.005	<0.01
r (mm)	>0.2	>0.3	>0.2	>0.3	>9	>9
$\hat{p}.\hat{r}$	>0.999	>0.999	0.999	>0.999	> 0.99995	0.999

Table 11.1: Summarised V^0 rejection constraints.

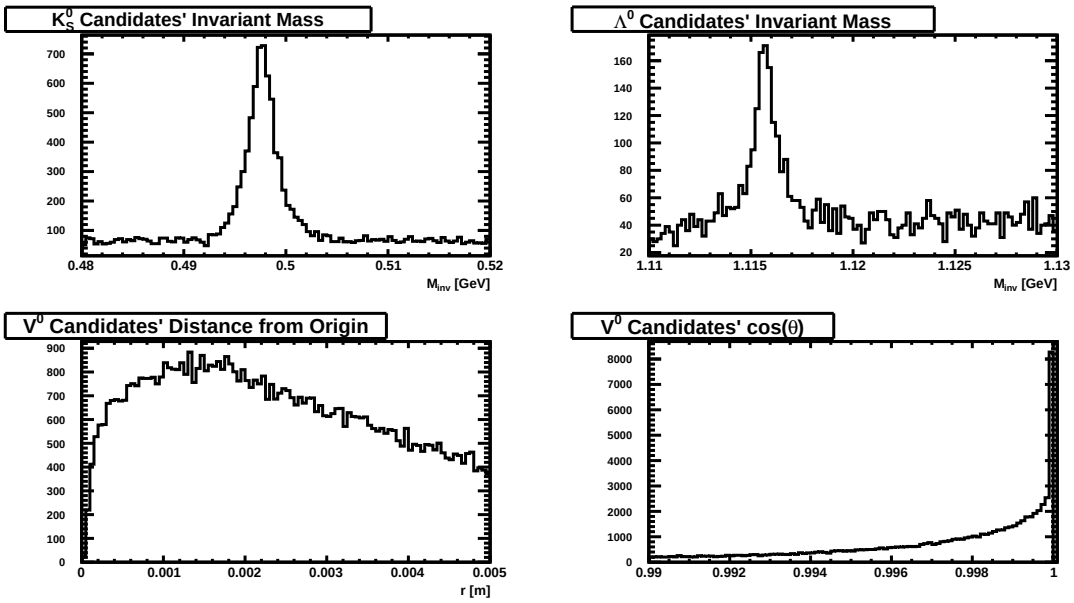

Figure 11.1: The three properties of the V^0 candidates in $Z \rightarrow b\bar{b}$ events, which are constrained to identify V^0 particles. The upper two plots show the invariant mass distributions in the ranges consistent with K^0_S and Λ^0 masses. The lower-left plot shows the distance of the candidate vertices from the origin and the lower-right plot shows the cosine of the angle between the radial vector of the vertex point and the momentum of the vertex; θ, in the plot, represents this angle

Since, V^0 particles decay to a pair of particles, to search for particle tracks originating from V^0 decay vertices, all possible pair of tracks are fitted to form two-track vertices. These vertices are referred to as V^0 candidates.

Three variables for these V^0 candidate vertices are calculated and subjected to constraints. The first is the invariant mass of the reconstructed vertex; the second is the distance between the the V^0 candidate vertex from the interaction point, denoted by r; and the third is the cosine of the angle between the momentum of the V^0 candidate vertex and the displacement vector from the interaction point to the V^0 candidate vertex position, denoted by $\hat{p}.\hat{r}$, which checks the consistency of whether the V^0 candidate particle originated at the primary vertex. Figure 11.1 shows the distributions of these variables for V^0 candidates for bottom flavoured decay events of the Z boson produced by the process presented in Chapter 8. It should be noted that the number of entries in the plot showing the invariant mass of Λ^0 candidates is twice as the others. This is because each possible pair of particles in consideration must be tested twice; once assuming one particle to be the proton and the other to be the π^-,

and again with the reverse ordering. The peaks in the invariant mass plots for the K^0_S and Λ^0 candidates indicate to the presence of these V^0 particles.

If all three variables of a reconstructed two-track vertex fall within the range of values compatible with one of the V^0 particle, the reconstructed vertex is denoted as a V^0.

There are two sets of selection constraints[29] that have been used to find V^0 particles, namely the 'tight' and the 'loose' constraints. These constraints are summarised in Table 11.1. If a reconstructed two-track vertex passes the 'tight' selection constraints, then the pair of tracks forming this vertex are entirely removed from the set of tracks used for finding secondary vertices. However, if a reconstructed two-track vertex passes the 'loose' selection constraints, then the pair of tracks forming this vertex are not used in the reconstruction of bottom or charm vertices but are not completely rejected and are considered with other tracks while forming other vertices.

12 Impact Parameter Tagging

The first flavour tagging algorithm to be presented is Impact Parameter Tagging, called so because this algorithm considers the transverse impact parameter of the particle tracks as the only tagging parameter to identify the event as the bottom, charm, or light flavoured decay channel of the Higgs boson or the particle being studied. This study presents the algorithm as a *b-tagging* algorithm, where b-tagging is defined as identifying the flavour of decay events to bottom quark. This algorithm can only be used after the two jets originated from the hadronic decay of the Higgs boson or the particle being studied in the process have been identified. Section 12.2 summarises the algorithm developed through the study presented in the following section.

12.1 Study

To study and review the performance of the Impact Parameter Tagging algorithm, hadronic decay events of the Z boson are simulated and the particle tracks are passed through the selection criteria as outlined in Chapter 8. The tracks used in this study are the tracks simulated in pythia and not the "observed" tracks obtained from the routine presented in Section 6.3.

All of the particle tracks that pass the selection are then clustered into two jets. FastJet was used to implement the `ee-kt algorithm` to group all the particle tracks into two separate jets. The detailed description of the clustering algorithm has been presented in Section 8.1.

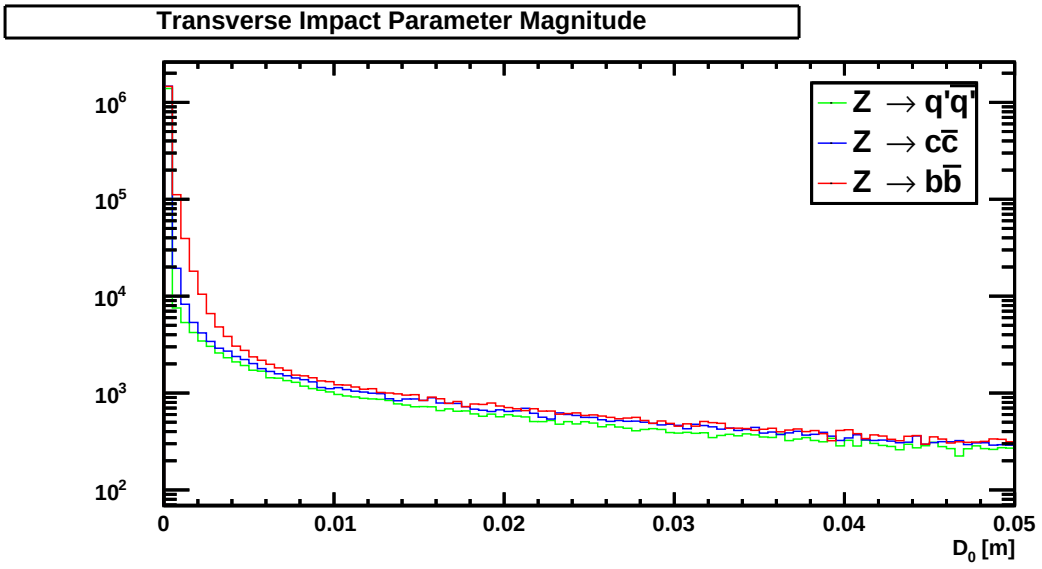

Figure 12.1: The magnitude of transverse impact parameters for $Z \to q\bar{q}$ events, with $q \equiv b$ shown in red, $q \equiv c$ shown in blue, and $q \equiv q' \equiv (u, d, s)$ shown in green. The distributions correspond to the $100{,}000$ events with $q \equiv b$, $q \equiv c$, and $q \equiv (u, d, s)$ each.

The particle tracks follow a helical trajectory in the magnetic field of the detector as defined in Chapter 6. These track equations can be described by the canonical track parameters and one of these parameters is the transverse impact parameter of the track, D_0. This transverse impact parameter is calculated for all particle tracks with respect to the interaction point, which, in this study, has been chosen as the origin of the coordinate system of the detector. For this algorithm, only the magnitude of the transverse impact parameter is required and the sign has no consequence. The distributions of the magnitudes of transverse impact parameters for $Z \to q\bar{q}$ events, with $q \equiv b, c, (u, d, s)$, are shown in Figure 12.1.

As can be seen in Figure 12.1, there are some particle tracks that have very large magnitudes of transverse impact parameters. The bottom quark has a significant lifetime, which results in finite magnitudes of transverse impact parameters for the tracks originating from the bottom hadron decay vertex, but the tracks with very large transverse impact parameters are particle tracks originating from the decay vertices of the V^0 particles. V^0 particles, as defined in Chapter 11, are the long-lived neutral particles, which decay in pairs of charged particles. A majority of the events constitute decay chains where the bottom hadron decays into a charm hadron which further decays to a light hadron. Particle tracks originating from these later vertices also have

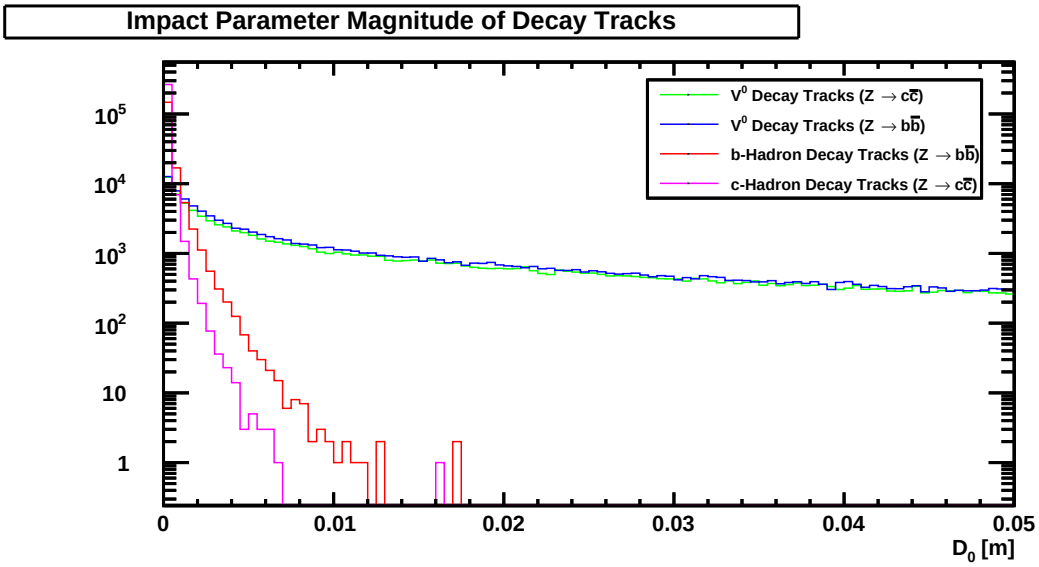

Figure 12.2: The magnitude of transverse impact parameters for tracks originating from bottom and charm hadrons and the V^0 particle decays for $Z \rightarrow q\bar{q}$ events, with distributions for $q \equiv b$ shown in red and blue, and for $q \equiv c$ shown in magenta and green. The distributions correspond to $100{,}000$ events with $q \equiv b$ and $q \equiv c$ each.

large transverse impact parameters. Figure 12.2 shows the different ranges of magnitude of transverse impact parameter for tracks originating from bottom and charm hadrons and the V^0 particles. Therefore, a threshold is put on the magnitudes of transverse impact parameters of the particle tracks to remove tracks originating from these V^0 vertices and only the tracks that have a transverse impact parameter magnitude smaller than the threshold value are retained in the jets and the rest of the tracks are excluded from the further flavour identification process.

This threshold value has to be carefully determined and optimised with regards to the efficiency and the accuracy of the flavour identification algorithm. In this study, this threshold is kept at 2.5 mm and the performance plots presented later in this section correspond to the same. If this threshold value is kept too high then a substantial number of particle tracks from V^0 decay vertices and from the later decays vertices of the hadronic decay chains are included in the set of particle tracks used for flavour identification. If the threshold is instead kept at 5 mm for the sample of $Z \rightarrow b\bar{b}$ events analysed in this study, the number of tracks originating from bottom hadron decays is only incremented by 0.73% than at the threshold value of 2.5 mm, while the number of tracks originating from the V^0 particle decays is incremented by 38.59%. This is likely

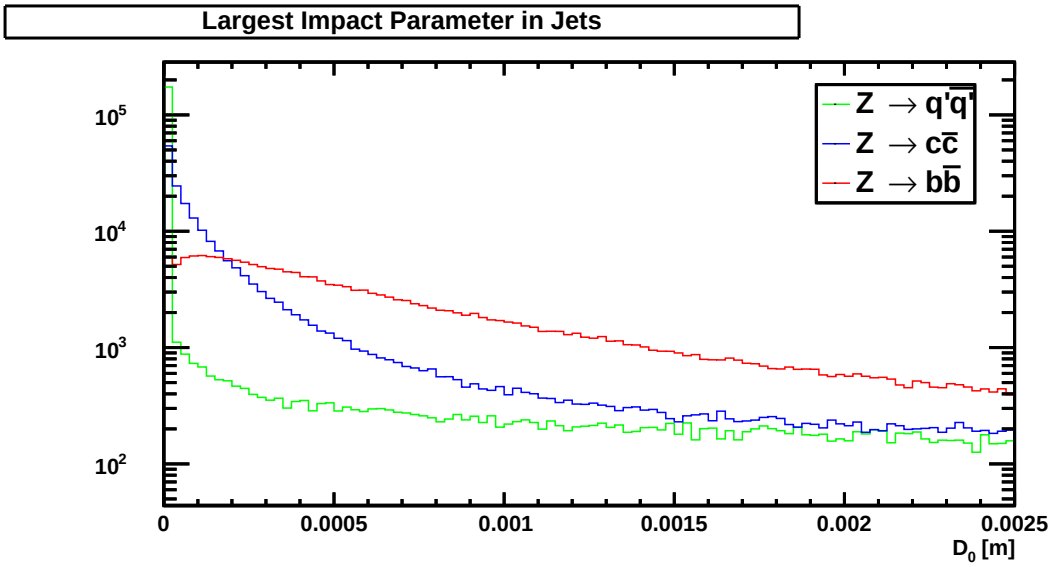

Figure 12.3: The largest impact parameter magnitude in individual jets after removing tracks with D_0 magnitude greater than 2.5 mm for the same sample of events as Figure 12.1, with $q = b$ shown in red, $q = c$ shown in blue, and $q = (u, d, s)$ shown in green.

to result in misidentification of $Z \to q'\bar{q}'$ events, with $q' \equiv (u, d, s)$, and $Z \to c\bar{c}$ events as $Z \to b\bar{b}$ events. However, if the threshold value is kept too low then an appreciable number of particle tracks from the first hadronic decay vertex may be discarded. If the threshold is reduced down to 1 mm for the sample of $Z \to b\bar{b}$ events, the tracks originating from bottom hadron decays are fewer by about 5% than at the threshold value of 2.5 mm. This may lead to misidentification of $Z \to b\bar{b}$ events and since a majority of tracks would be discarded, the flavour identification would not be reliable. Figure 12.9 presents the plots showing the efficiency and accuracy of the classification of the events for two different values of this threshold.

The magnitudes of transverse impact parameters of all the remaining particle tracks form the data-set which is used to calculate the tagging parameter. The largest transverse impact parameter in each jet is found among all the remaining particle tracks. The distributions of the largest transverse impact parameter magnitude from each jet for $Z \to q\bar{q}$ events, with $q \equiv b, c, (u, d, s)$, are shown in Figure 12.3.

A distinguishing pattern in the three distributions can be identified from Figure 12.3. For $Z \to b\bar{b}$ events, the distribution peaks a little farther from zero owing to the longer lifetimes of the bottom hadrons while the distribution for

$Z \to q'\bar{q}'$ events, with $q' \equiv (u, d, s)$, peaks very close to zero and flattens our very quickly. The distribution for $Z \to c\bar{c}$ events also has a peak close to zero but it is a wider distribution than that for $Z \to q'\bar{q}'$ events, with $q' \equiv (u, d, s)$.

This difference can be used to define a threshold, which can be used to classify events as $Z \to b\bar{b}$, $Z \to c\bar{c}$, or $Z \to q'\bar{q}'$ events, with $q' \equiv (u, d, s)$. Particle tracks from a single hemisphere can be used for this purpose and the largest transverse impact parameter magnitude in that hemisphere can be used as the tagging parameter. For an efficiency of 80% to correctly identify $Z \to b\bar{b}$ events using this tagging threshold, the rate of misidentification of $Z \to c\bar{c}$ events was measured to be 34.66% and that for $Z \to q'\bar{q}'$ events, with $q' \equiv (u, d, s)$ was measured to be 10.88%.

The entire event can also be used in the flavour identification process. Instead of using the particle tracks from only one hemisphere, particle tracks from both hemispheres can be used. This, of course, has the technical advantage that jet clustering is not required before the flavour tagging process. The largest transverse impact parameter magnitude in the event, rather than one hemisphere, is used as the tagging parameter and a threshold can be chosen to classify events as $Z \to b\bar{b}$, $Z \to c\bar{c}$, or $Z \to q'\bar{q}'$ events, with $q' \equiv (u, d, s)$. For an efficiency of 80% to correctly identify $Z \to b\bar{b}$ events, the rate of misidentification of $Z \to c\bar{c}$ events while using this tagging threshold was measured to be 30.96% and that for $Z \to q'\bar{q}'$ events, with $q' \equiv (u, d, s)$ was measured to be 16.89%. This tagging threshold has lesser contamination from $Z \to c\bar{c}$ events but higher contamination from $Z \to q'\bar{q}'$ events, with $q' \equiv (u, d, s)$ than when particle tracks from a single hemisphere are used. The misidentification of the $Z \to q'\bar{q}'$ events, with $q' \equiv (u, d, s)$ as $Z \to b\bar{b}$ and $Z \to c\bar{c}$ events can be reduced remarkably by using a different tagging parameter, which is described below.

Considering the largest transverse impact parameters from each jet of the event, there are two data points for each event. A two-dimensional distribution can be created with each axis representing the largest transverse impact parameter magnitude in one hemisphere and each event represented by a point in this space. This distribution is, naturally, very chaotic and no workable distinguishing features can be recognised to classify the events into different flavours.

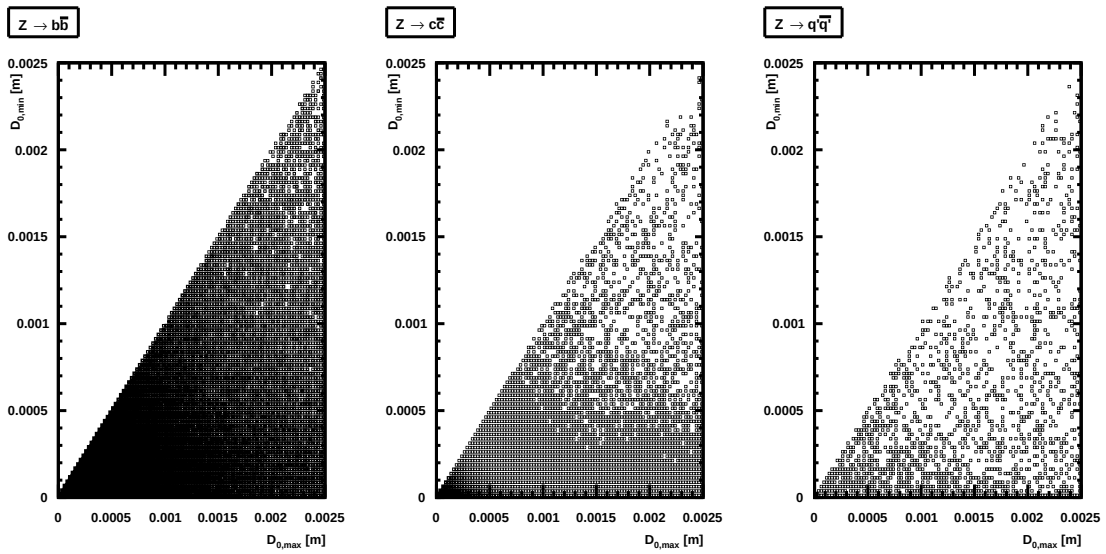

Figure 12.4: The distribution of events in the space of $D_{0,min}$ and $D_{0,max}$ for the same sample of $Z \to q\bar{q}$ events, with $q \equiv b, c, (u, d, s)$, as Figure 12.1. $D_{0,min}$ and $D_{0,max}$ are respectively the minimum and the maximum of the largest transverse impact parameters in the two jets of the events

But, when the minimum and the maximum of the largest transverse impact parameter magnitudes from each jet are calculated and the axes of the distribution are replaced by these two values, in place of the previous two absolute data points, some distinguishing features start to arise. This distribution is shown in Figure 12.4. It can be seen that most of the $Z \to q'\bar{q}'$ events, with $q' \equiv (u, d, s)$, are clustered on the x-axis, which represents the maximum of the largest transverse impact parameter magnitude from each jet. This indicates that the minimum of these two transverse impact parameter magnitudes from each event is very small for the majority of the $Z \to q'\bar{q}'$ events, with $q' \equiv (u, d, s)$. Thus if the minimum of the largest transverse impact parameter magnitudes from each jet of the event is used to classify the events, it will ensure that fewer $Z \to q'\bar{q}'$ events, with $q' \equiv (u, d, s)$ are misidentified as $Z \to b\bar{b}$ or $Z \to c\bar{c}$ events. Thus, it was chosen as the tagging parameter in this study of the Impact Parameter Algorithm.

The distribution of the tagging parameters for $Z \to q\bar{q}$ events, with $q \equiv b, c, (u, d, s)$, can be seen in Figure 12.5. The distinguishing features of these distributions can be observed clearly. The distribution for $Z \to b\bar{b}$ events peaks at a higher value than the distributions for the $Z \to c\bar{c}$ and $Z \to q'\bar{q}'$ events, with $q' \equiv (u, d, s)$. It is also broader than the other two, signifying that the tagging parameter for the majority of the $Z \to b\bar{b}$ events is significantly higher

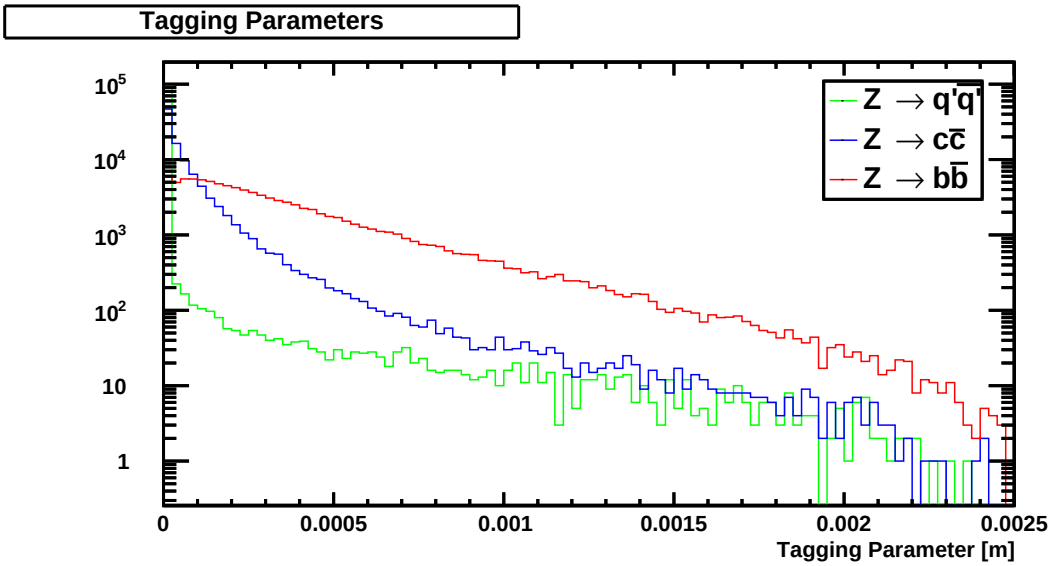

Figure 12.5: The distribution of tagging parameter for the same sample of $Z \to q\bar{q}$ events as Figure 12.1, with $q \equiv b$ in red, $q \equiv c$ in blue, and $q \equiv (u, d, s)$ in green.

than that for the majority of $Z \to c\bar{c}$ and $Z \to q'\bar{q}'$ events, with $q' \equiv (u, d, s)$. At the same time, the distribution for $Z \to q'\bar{q}'$ events, with $q' \equiv (u, d, s)$, peaks very close to zero and dies very quickly, i.e. the tail of the distribution is negligible compared to that for $Z \to b\bar{b}$ events.

A cumulative distribution can be plotted from the distribution of tagging parameters, which will illustrate how many events have a tagging parameter bigger than a particular value. This is presented in Figure 12.6, where the x-axis depicts the tagging parameter values. The cumulative distribution for the $Z \to b\bar{b}$ events is considerably broader than for the $Z \to c\bar{c}$ events. For the $Z \to q'\bar{q}'$ events, with $q' \equiv (u, d, s)$, the cumulative distribution dies away fast; this, again, demonstrates that the chosen tagging parameter is likely to have very small impurity from $Z \to q'\bar{q}'$ events, with $q' \equiv (u, d, s)$ in the flavour identification of the $Z \to b\bar{b}$ events. A tagging threshold can be chosen using these distributions that is compatible with a required efficiency.

These cumulative distributions for $Z \to q\bar{q}$ events, with $q \equiv b, c, (u, d, s)$, can be used to produce ROC curves, with efficiency and accuracy of identification representing the two axes. The ROC curve for the $Z \to b\bar{b}$ and $Z \to c\bar{c}$ events is shown in Figure 12.7; the ROC curve for the $Z \to b\bar{b}$ and $Z \to q'\bar{q}'$ events, with $q' \equiv (u, d, s)$, is shown in Figure 12.8. These curves can be used to decide

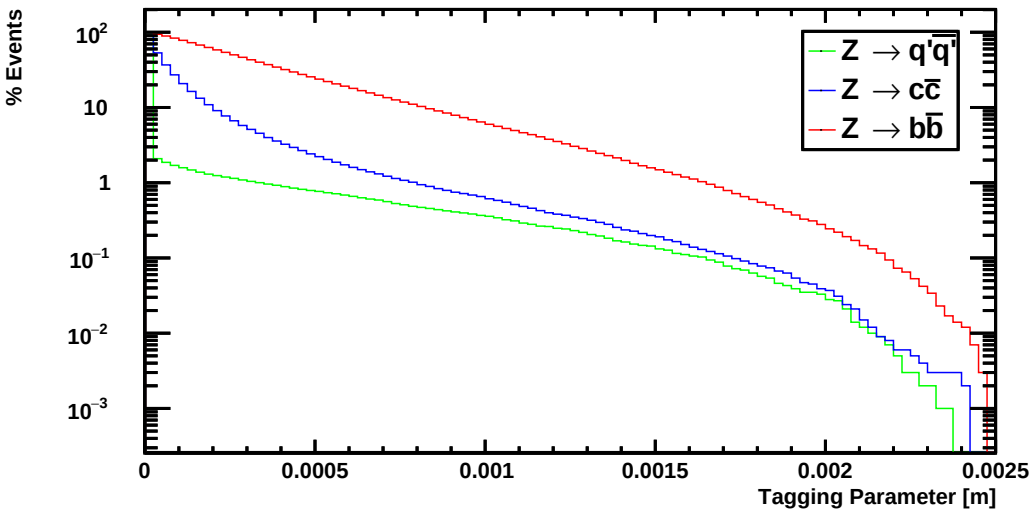

Figure 12.6: Percentage of events with transverse impact parameter magnitude greater than a tagging parameter as a function of the tagging parameter for the same sample of $Z \to q\bar{q}$ events as Figure 12.1, with $q \equiv b$ in red, $q \equiv c$ in blue, and $q \equiv (u, d, s)$ in green.

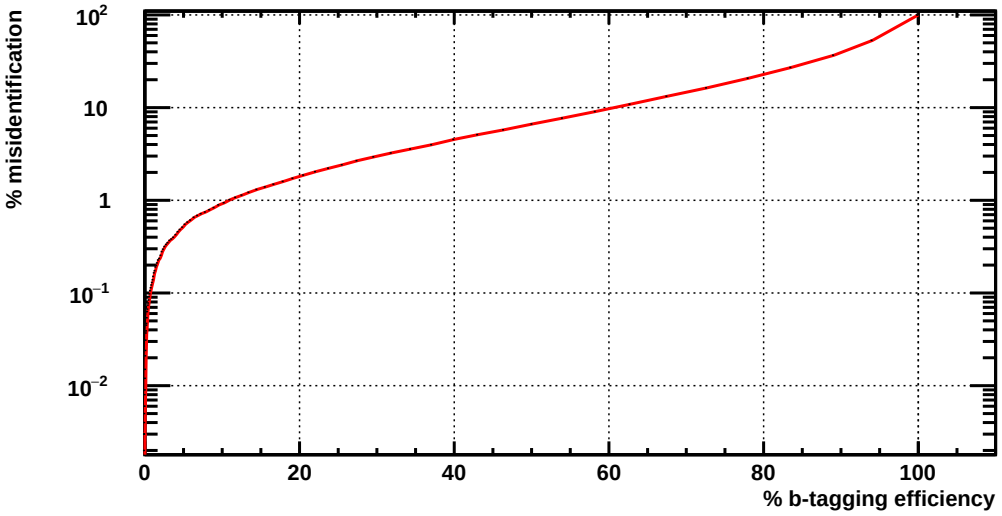

Figure 12.7: Efficiency of identifying $Z \to b\bar{b}$ events with a rate of misidentification of $Z \to c\bar{c}$ events.

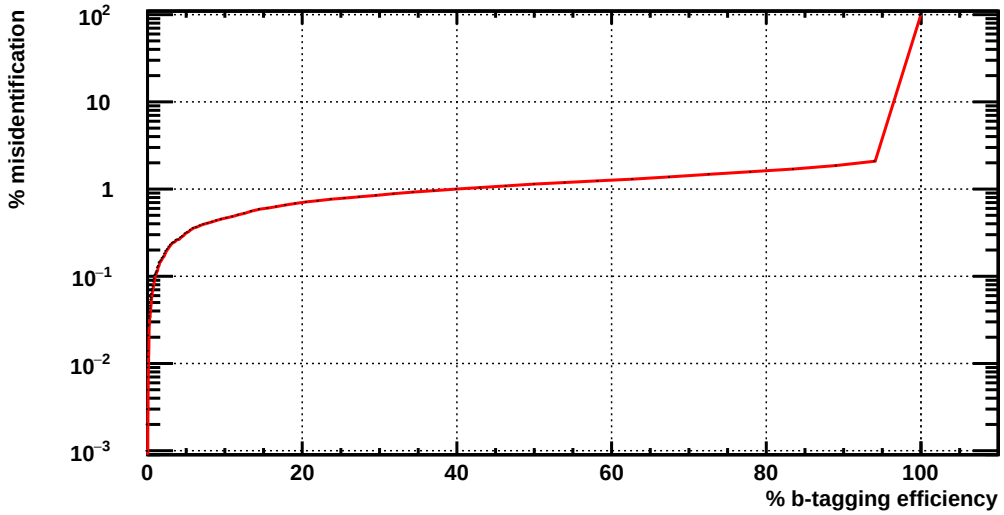

Figure 12.8: Efficiency of identifying $Z \to b\bar{b}$ events with a rate of misidentification of $Z \to q'\bar{q}'$ events, with $q' \equiv (u, d, s)$.

the threshold that will be used to identify and classify events as being $Z \to b\bar{b}$. While determining this threshold two things are considered; the efficiency of identification, i.e. the percentage of $Z \to b\bar{b}$ events that are accurately identified; and the inaccuracy of identification, i.e. the percentage of $Z \to c\bar{c}$ or $Z \to q'\bar{q}'$ events, with $q' \equiv (u, d, s)$ that are erroneously identified as $Z \to b\bar{b}$ events. A tagging threshold is then chosen to get a particular efficiency of identification corresponding to a reasonable inaccuracy of identification.

Another function of the ROC curves is to optimise all the thresholds used in the entire flavour-tagging algorithm. Figure 12.9 shows the curves for $Z \to b\bar{b}$ and $Z \to c\bar{c}$ events for different values of threshold cut on the transverse impact parameter magnitude of all final particle tracks, particle tracks with transverse impact parameter magnitude greater than which were discarded from the set of tracks used for the tagging algorithm. The optimum value of this threshold cut is the one for which the ROC curve is the closest to the top-right corner. As can be seen, a threshold value of 2.5 mm optimises the performance of this algorithm, thus it was chosen in this study.

A point on the ROC curve of $Z \to b\bar{b}$ and $Z \to c\bar{c}$ events is chosen to determine the tagging threshold. The chosen point indicates the best efficiency of accurate identification of $Z \to b\bar{b}$ events possible and the corresponding misidentification rate of $Z \to c\bar{c}$ events as $Z \to b\bar{b}$ events that can be expected.

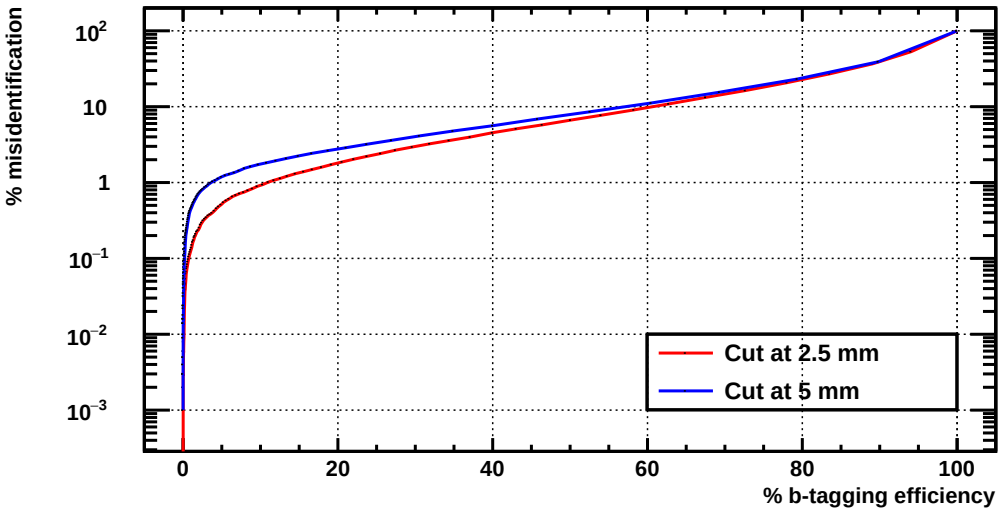

Figure 12.9: The efficiency of identifying $Z \to b\bar{b}$ events with the rate of misidentification of $Z \to c\bar{c}$ events for two different thresholds on transverse impact parameter magnitude.

The ROC curve of $Z \to b\bar{b}$ and $Z \to q'\bar{q}'$ events, with $q' \equiv (u, d, s)$, indicates the corresponding misidentification rate of $Z \to q'\bar{q}'$ events, with $q' \equiv (u, d, s)$, as $Z \to b\bar{b}$ events that can be expected. Then the cumulative distribution of the tagging parameter is used to find the tagging threshold corresponding to the required efficiency of identification of $Z \to b\bar{b}$ events.

For a tagging threshold value of 115 microns, the best achievable efficiency of accurate identification of the $Z \to b\bar{b}$ events is 80%. The rate of misidentification of $Z \to c\bar{c}$ events as $Z \to b\bar{b}$ events for this efficiency was found to be 23.16% and the rate of misidentification of $Z \to q'\bar{q}'$ events, with $q' \equiv (u, d, s)$, as $Z \to b\bar{b}$ events was found to be 1.74%.

12.2 Algorithm

Summarising the analysis presented in the preceding section, the following steps are followed to identify a bottom flavoured event:

- All the final particle tracks are clustered separately into two jets.
- The absolute magnitude of the signed transverse impact parameter, D_0, for all the particle tracks is calculated.

- To suppress V^0 decay tracks, all the particle tracks that have a transverse impact parameter magnitude greater than a threshold value are removed from the jets and are not considered in the further tagging process.
- Among the remaining particle tracks from each hemisphere, the tracks with the largest transverse impact parameter magnitudes are found along with their corresponding transverse impact parameter magnitude.
- The smaller of these two transverse impact parameter magnitudes is chosen as the tagging parameter.
- The tagging parameter is compared with a predetermined tagging threshold value. If this tagging parameter is greater than the tagging threshold value then the event is classified as a bottom flavoured event.

This tagging threshold value for classifying the event is set depending on the efficiency and purity of identification required. The optimum value for this tagging threshold to classify bottom flavoured events corresponds to the best efficiency for correct identification of the events and the fewest possible misidentification of charm or light flavoured events as bottom flavoured events.

12.3 Conclusion

The results reported in Table 12.1 correspond to the threshold value of 2.5 mm on the magnitude of the transverse impact parameter for particle tracks to be accepted in the flavour tagging process.

b - tagging parameter	c - misidentification	(u, d, s) - misidentification
t_1	34.66%	10.88%
t_2	30.96%	16.89%
t_3	23.16%	1.74%

Table 12.1: The rate of misidentification of $Z \to c\bar{c}$ events and $Z \to q'\bar{q}'$ events, with $q' \equiv (u, d, s)$, as $Z \to b\bar{b}$ events using three different tagging parameters, corresponding to an 80% efficiency of identification of $Z \to b\bar{b}$ events. t_1 represents the largest transverse impact parameter magnitude from a single jet in the event chosen as the tagging parameter; t_2 represents the largest transverse impact parameter magnitude from the event chosen as the tagging parameter; t_3 represents the minimum of the largest impact parameter from each jet of the event chosen as the tagging parameter.

As demonstrated in Table 12.1, using the minimum of the largest impact parameter magnitudes from each jet, or t_3, as the tagging parameter reduces the rate of misidentification of $Z \to q'\bar{q}'$ events, with $q' \equiv (u, d, s)$, considerably.

A few suggestions for follow-up studies to improve on these results are suggested in Chapter 15.

13 Soft Lepton Taggers

The bottom and the charm quark can decay semi-leptonically to a muon or an electron, and the bottom quark can also decay semi-leptonically via the charm quark. These processes, if resulting in a muon, can be represented as following,

$$\begin{aligned} b &\to \mu\nu_\mu X \\ c &\to \mu\nu_\mu X \\ b &\to c \to \mu\nu_\mu X \end{aligned} \tag{13.1}$$

These muons are also refered to as soft lepton taggers. As the masses of the bottom and the charm quark, and therefore their corresponding hadrons, are significantly different, the momentum perpendicular to the direction of motion of the mother particle of the muons originating in such decays will also be different. This property can be used to distinguish between the two quark flavours. Events with semi-leptonic decays to electrons can also be used for this purpose, however, this gives a lower performance. The soft lepton taggers are not used to identify hadronic decay channels directly but are rather used to improve the efficiency of identification in other methods.

13.1 Study

To study these soft lepton taggers, $Z \to b\bar{b}$ and $Z \to c\bar{c}$ events were produced in e^+e^- collisions and selection constraints were applied on the resulting particles as described in Chapter 8. The particles obtained after the selection

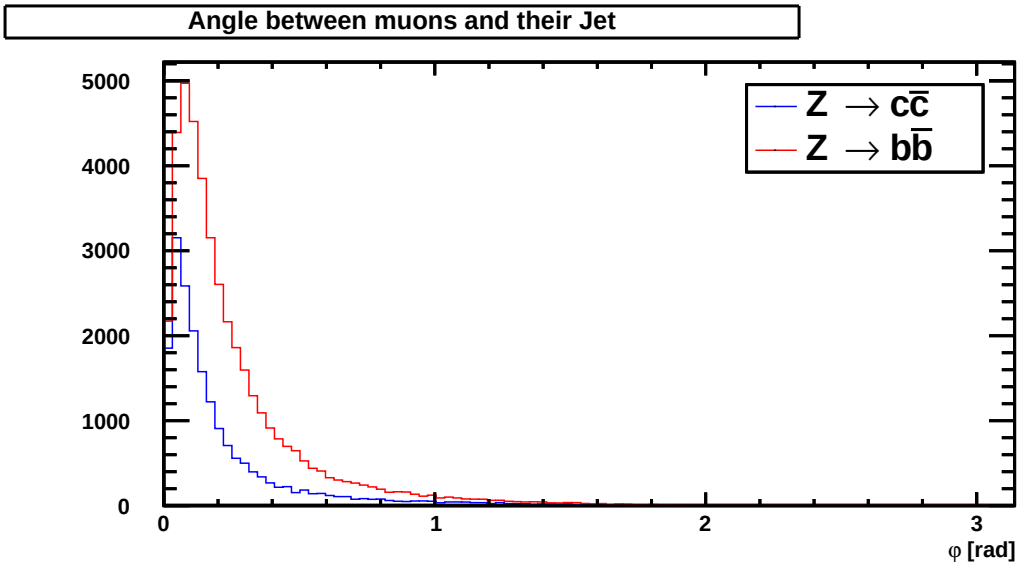

Figure 13.1: Angle between the the momentum of the muons and their corresponding jet axis for $Z \to q\bar{q}$ events, with $q \equiv b$ in red, $q \equiv c$ in blue. The distributions correspond to $100{,}000$ events with $q \equiv b$ and $q \equiv c$ each.

were clustered into two jets with the `ee-kt algorithm` described in Section 8.1.

For $Z \to b\bar{b}$ events, muons originating from the semi-leptonic decays of the bottom hadrons, direct and via charm hadrons, are detected. For $Z \to c\bar{c}$ events, muons originating from the direct semi-leptonic decay of the charm hadron are identified. The angle between these muons and their corresponding jet is then calculated. Figure 13.1 shows the distributions of these angles for two of the three different cases. The distribution for muons produced from the direct semi-leptonic decay of the bottom hadrons is broader than the other case, which suggests that these muons have higher momenta in the direction perpendicular to their corresponding jet axis.

As stated above, the bottom hadrons have considerably higher masses than the charm hadrons. Thus, a muon resulting from the semi-leptonic decay of a bottom hadron is likely to have a higher momentum in the direction perpendicular to the direction of travel of the hadron than a muon produced from the semi-leptonic decay of a charm hadron. This is what is apparent in the distributions presented in Figure 13.2, which depict the relative momentum of the muons transverse to their corresponding jet axis for the three processes in Equation 13.1. The distribution for the muons produced from the semi-leptonic

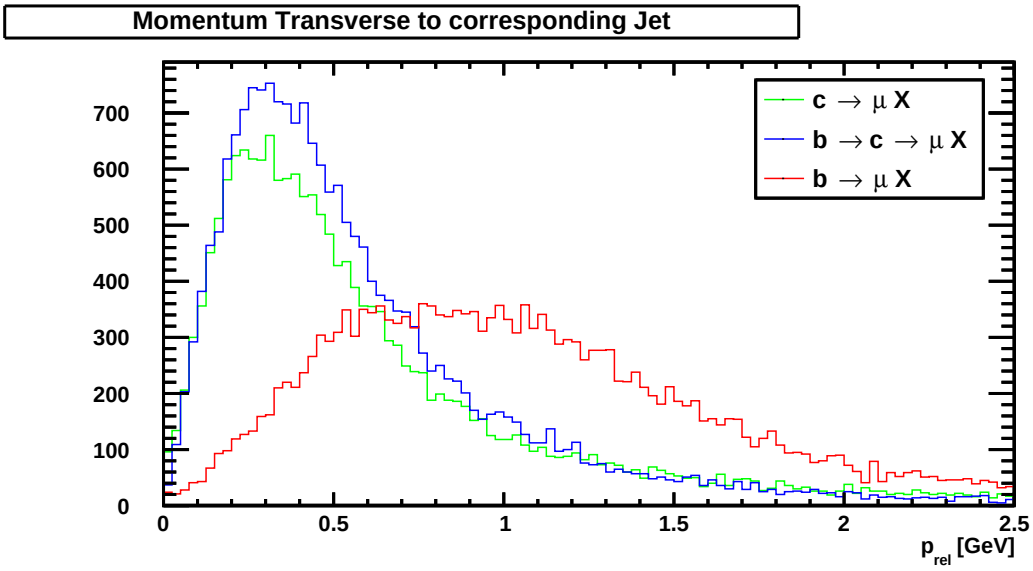

Figure 13.2: The magnitudes of the relative momentum of muons transverse to their jet axis for the direct (in red) and via charm (in blue) semi-leptonic decays of bottom quark, and direct (in green) semi-leptonic decays of charm quarks in $Z \to q\bar{q}$ events, corresponding to $100{,}000$ events with $q \equiv b$ and $q \equiv c$ each.

decay of bottom hadrons peaks later and is broader than for the other two processes. This feature can be used to distinguish between the bottom and charm hadron events.

The soft lepton taggers can be used to reject the $Z \to q'\bar{q}'$ events, with $q' \equiv (u, d, s)$, that have been misidentified as $Z \to b\bar{b}$ or $Z \to c\bar{c}$ events. At the same time, it can also be used to correctly classify some of the $Z \to c\bar{c}$ events that have been misidentified as $Z \to b\bar{b}$ events.

14 Flavour Tagging through Secondary Vertex Reconstruction

Finding secondary vertices, as defined in Chapter 10, is a vital step in a precise flavour identification process. The first section reports the study of hadronic decay events of the Z boson with the aim to classify the decay jets into four categories, defined later, which can further be used to identify the hadronic flavour of the event. Section 14.3 summarises this analysis into an algorithm that can be employed to classify decay jets into these four categories.

14.1 Study

To classify events by reconstructing secondary vertices, events for the reaction $e^+e^- \rightarrow Z \rightarrow q\bar{q}$ were generated using the procedure outlined in Chapter 8, separately for $q = b, c, (u, d, s)$. All of the generated particle tracks were subjected to the selection conditions stated in Chapter 8 and track parametrisation was performed on the final set of simulated particle tracks using the routine mentioned in Section 6.3 to obtain the corresponding "observed" tracks.

All the vertex fits are performed using the algorithm presented in Chapter 7.

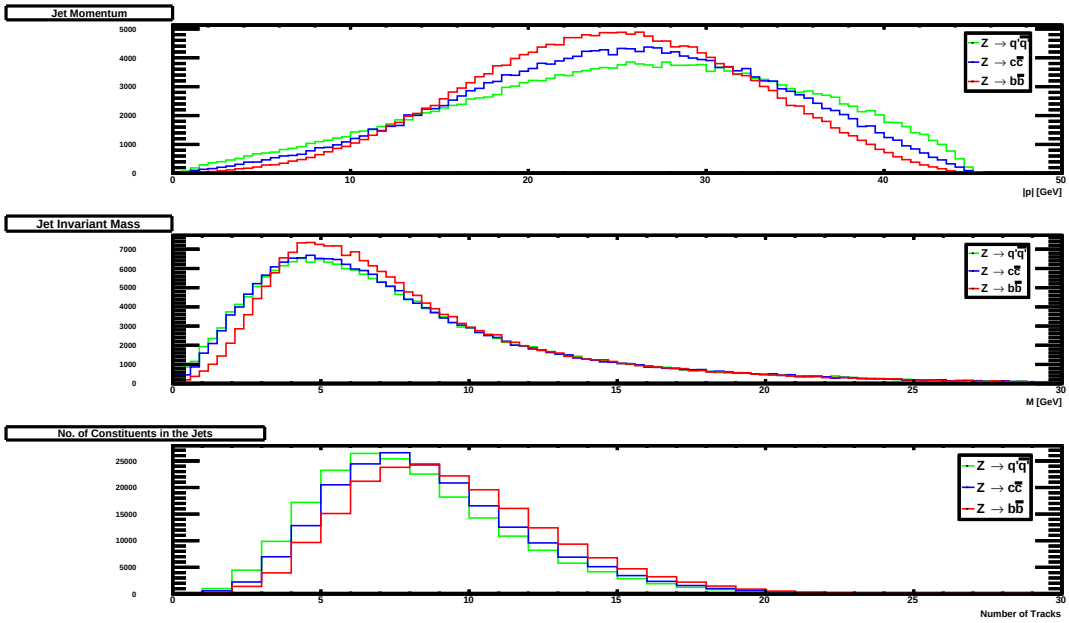

Figure 14.1: Reconstructed jets in $Z \to q\bar{q}$ events using only charged tracks, with $q \equiv b$ shown in red, $q \equiv c$ shown in blue, and $q \equiv q' \equiv (u, d, s)$ shown in green. The distributions correspond to the $10{,}000$ events with $q \equiv b$, $q \equiv c$, and $q \equiv (u, d, s)$: The first plot shows the magnitude of the momentum, the second plot shows the invariant mass, and the third plot shows the track multiplicity of the jets.

14.1.1 Jet Clustering

All the "observed" tracks were clustered into separate jets with FastJet by using the `ee-kt algorithm`, which has been detailed in Section 8.1. Since the simulated events are di-jet events, the number of jets specified to the algorithm was two.

Figure 14.1 shows the distribution of the momentum, the invariant mass, and the track multiplicity of the jets for $Z \to q\bar{q}$ events.

As suggested in LCFIPlus, the order of the two steps of jet clustering and vertex finding can be reversed. If jet clustering is performed after finding secondary vertices, then these vertices, along with the muon tracks from the semi-leptonic decays can be used as seeds in a modified clustering algorithm[31]. This has an advantage over the traditional method of performing jet clustering before finding vertices, which is that the tracks from a common decay vertex can sometimes mistakenly be clustered in different jets and that would make finding that vertex from fitting tracks from individual jets harder or, in some

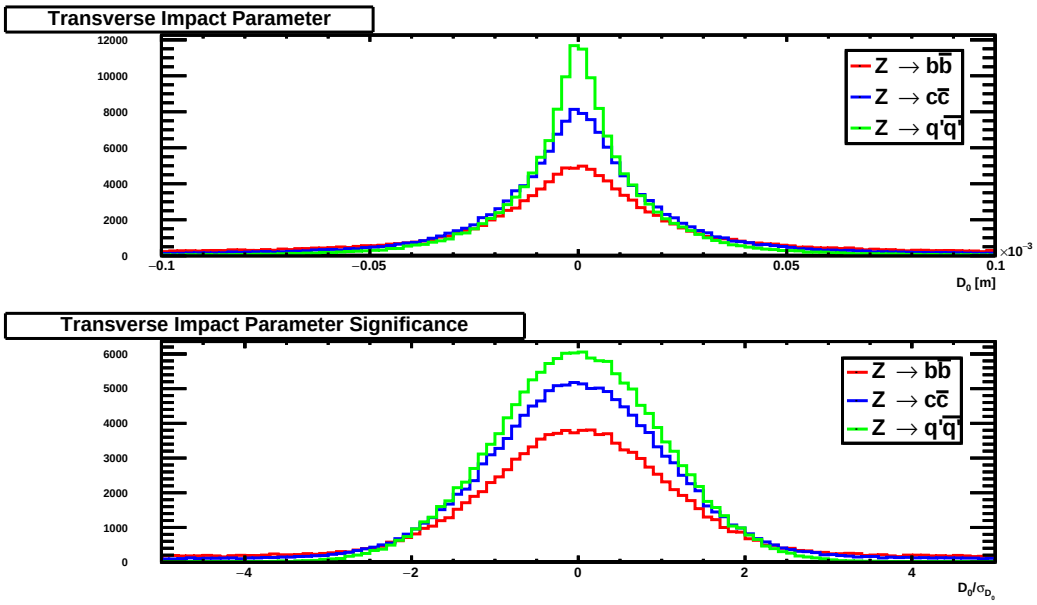

Figure 14.2: Signed impact parameter and impact parameter significance of charged tracks for the same sample of $Z \to q\bar{q}$ events as Figure 14.1, with $q \equiv b$ shown in red, $q \equiv c$ shown in blue, and $q \equiv q' \equiv (u, d, s)$ shown in green.

instants, even impossible. There are increased chances of this happening in a multi-jet event with three or more jets. However the events analysed in this study are di-jet events with the two jets being in opposite directions, and this effect is expected to be insignificant. Therefore, in order to simplify the algorithm, the order used here is clustering all of the tracks into two jets first and then finding vertices. The reported results of its performance correspond to the same order.

All of the steps after this, with the exception of finding primary vertex, are performed for each jet separately.

14.1.2 Primary Vertex Finding

A very straightforward approach has been presented here to find the primary vertex of the event. The essential purpose of finding the primary vertex is to remove the tracks that are compatible with having originated from the primary vertex from the secondary vertex search. The tracks which are classified as those forming the primary vertex are referred to here as primary tracks and the rest of the tracks are referred to as non-primary tracks.

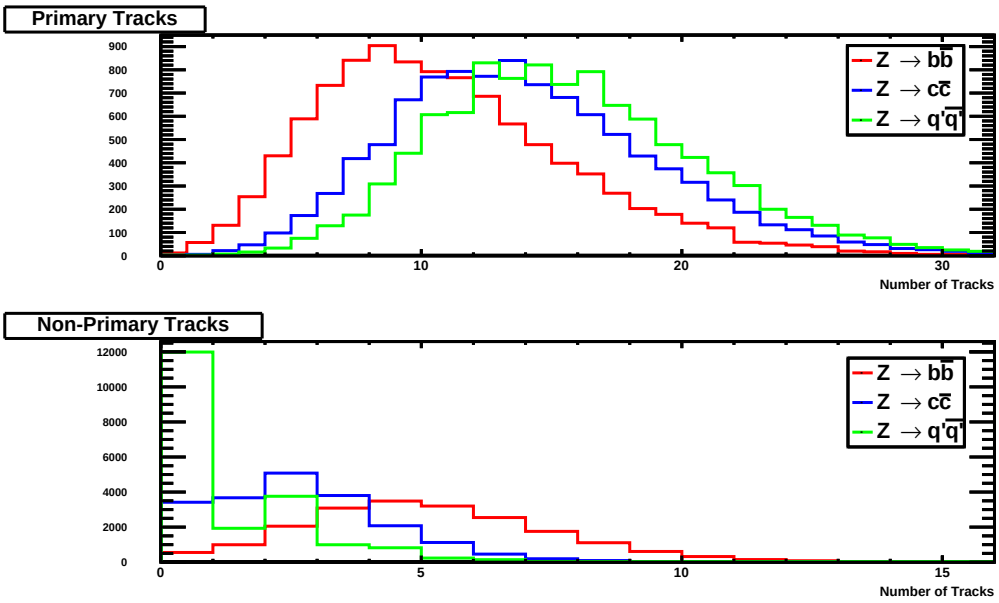

Figure 14.3: Number of primary and non-primary tracks per jet for the same sample of $Z \to q\bar{q}$ events as Figure 14.1, with $q \equiv b$ shown in red, $q \equiv c$ shown in blue, and $q \equiv q' \equiv (u, d, s)$ shown in green.

To separate these two kinds of track, the transverse impact parameter significance (S_{D_0}) was calculated for each track. Transverse impact parameter significance is defined as,

$$S(D_0) = \frac{D_0}{\sigma_{D_0}}, \tag{14.1}$$

where D_0 is the transverse impact parameter and σ_{D_0} is its uncertainty. The distributions of the transverse impact parameter and its significance for the tracks in $Z \to q\bar{q}$ events are shown in Figure 14.2. Tracks that had a transverse impact parameter significance within a threshold range were classified as primary tracks and the rest of the tracks were classified as non-primary tracks. This threshold range was chosen to be $[-3, 3]$. The track multiplicity for primary and non-primary tracks for $Z \to q\bar{q}$ events is shown in Figure 14.3.

The primary tracks were fitted to a common vertex using the vertex fitting algorithm. Figure 14.4 shows the distributions of the coordinates, the radial distance of the fitted primary vertex and the associated χ^2 value for the vertex for $Z \to b\bar{b}$ events. The χ^2 values of the fitted primary vertices were used to optimise the threshold range stated above.

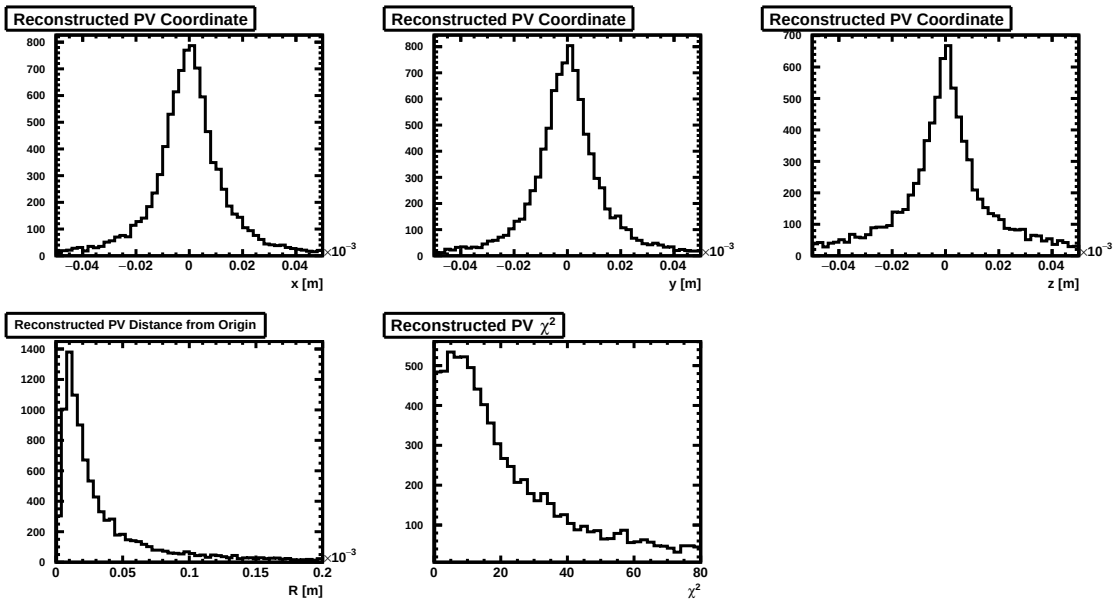

Figure 14.4: Primary Vertex: The coordinates and the distance with respect to origin, of the reconstructed primary vertices for the same sample of $Z \to b\bar{b}$ events as Figure 14.1. The last plot shows the χ^2 value of the vertex fit. PV stands for Primary Vertex.

14.1.3 Secondary Vertex Finding

After the tracks have been separated into primary and non-primary tracks, the non-primary tracks in each jet were used to find secondary vertices. V^0 rejection with the set of 'tight' constraints, as detailed in Chapter 11, was performed on the set of non-primary tracks. The pairs of tracks that were identified as forming a V^0 vertex, consistent with these constraints, were removed from the vertex finding procedure.

From the rest of the non-primary tracks, all possible track pairs were fitted to obtain a vertex for each track pair. These two-track vertices were subjected to the following constraints.

- The χ^2 value of the two-track vertex must be smaller than a threshold value.
- The invariant mass of the two-track vertex must be smaller than a threshold value.
- The track pair are subjected to V^0 rejection with the set of 'loose' constraints. Vertex candidates that pass the rejection are discarded.

- The direction of the displacement vector from the primary vertex to the two-track vertex and the direction of the sum of the two track momenta must be in the same hemisphere.

Out of all the reconstructed two-track vertices passing the selection, the vertex with the lowest χ^2 value was selected as the seed vertex for the secondary vertex finding algorithm. The threshold value for the vertex χ^2 was chosen to be 9 and the threshold value for the invariant mass of the vertex was chosen to be 10 GeV.

Once the best two-track vertex was found, additional tracks were attempted to be attached to this seed vertex to create a vertex with a higher track multiplicity. A track was added to the seed vertex if the χ^2 contribution of the track in the resulting vertex was smaller than a threshold value, chosen to be 5, and the resulting vertex qualified the constraints on the invariant mass, the position and the χ^2 value as mentioned above. Only two-track vertices are subjected to the V^0 selection, so it was not a requirement on the resulting vertex from adding a track to the seed vertex. Out of all the tracks which passed the selection constraints, the track, which resulted in a lowest vertex χ^2 value was chosen and added to the seed vertex.

This process was iterated to further add more tracks to the vertex until no more tracks could be combined to the vertex following the aforementioned criteria.

Once a secondary vertex was found, the set of tracks forming this vertex were removed and the entire procedure was then repeated to find further secondary vertices from the remaining tracks. Secondary vertices were reconstructed until no seed vertices could be found.

The number of secondary vertices found per jet, and the track multiplicity and the invariant mass of these secondary vertices for $Z \to q\bar{q}$ events are shown in Figure 14.5.

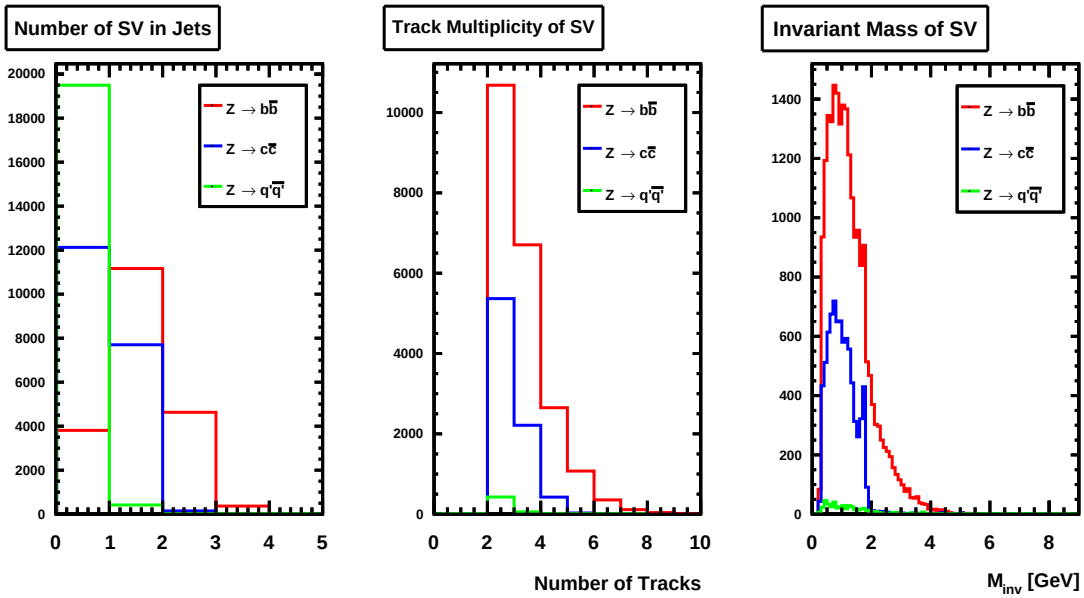

Figure 14.5: Secondary vertices: The number of secondary vertices found per jet, the track multiplicity and the invariant mass of the reconstructed secondary vertices for the same sample of $Z \to q\bar{q}$ events as Figure 14.1, with $q \equiv b$ shown in red, $q \equiv c$ shown in blue, and $q \equiv q' \equiv (u, d, s)$ shown in green. SV stands for secondary vertices.

14.1.4 Jet Vertex Refining

The purpose of vertex refining is to improve the distinction between the bottom and the charm flavoured events by reconstructing the number of secondary vertices as accurately as possible. If a jet has two secondary vertices, it is a strong indication of the event being a $Z \to b\bar{b}$ event. By employing the vertex refining step, the contamination from the events of a different flavour are tried to be minimised and some jets from $Z \to b\bar{b}$ events which have less than two secondary vertices are tried to be extracted in a separate category and identified.

The two steps performed during jet vertex refining were vertex combining and finding single-track vertex, which are defined below.

Vertex Combining

Vertex combining was performed for the jets which have three or more reconstructed secondary vertices to reduce the number of secondary vertices by combining neighboring vertices. The steps performed proceed as follows:

- Select a pair of secondary vertices.
- List all the tracks forming all the other secondary vertices in the jet.
- Add each of these tracks to each of the two selected secondary vertices and adopt the track-vertex combination in which the track has a smaller χ^2 contribution in the refitted vertex.
- Once all of the tracks from the list are attached to one or the other of the selected secondary vertices, compute the sum of χ^2 values of the two refitted vertices.
- Repeat this process with all possible pairs of secondary vertices and adopt the result that has the smallest χ^2 sum.

A further step can be added after this. In the jets with two secondary vertices, all the tracks from these two vertices can be combined into a single vertex and if the resulting vertex passes certain criteria, then the resulting single vertex is kept instead of the two vertices. For simplicity, this step was excluded from the analysis.

Finding Single-Track Vertices

The cascade of decays in the jets from $Z \to b\bar{b}$ events generally result in decay vertices that are nearly collinear with the primary vertex. There is a possibility of the presence of a single track that may have originated in an additional secondary decay. If there is such a track, it is referred to as a *pseudo-vertex*. Pseudo-vertices were found among the unassociated tracks of a jet, which are the non-primary tracks that are not part of any reconstructed vertex. This step can be performed on all jets but in this study, it has only been implemented for jets which have only one reconstructed secondary vertex. Figure 14.6 shows the track multiplicity for these unassociated tracks in the jets from $Z \to b\bar{b}$ events, with a single secondary vertex.

For a track to be classified as a pseudo-vertex, it was needed to satisfy the following set of criteria:

- The track must have either the transverse impact parameter significance (S_{D_0}) or the longitudinal impact parameter significance (S_{z_0}) greater than 5.
- The opening angle between the vertex line, defined as the line joining the primary vertex and the secondary vertex, and the track direction at

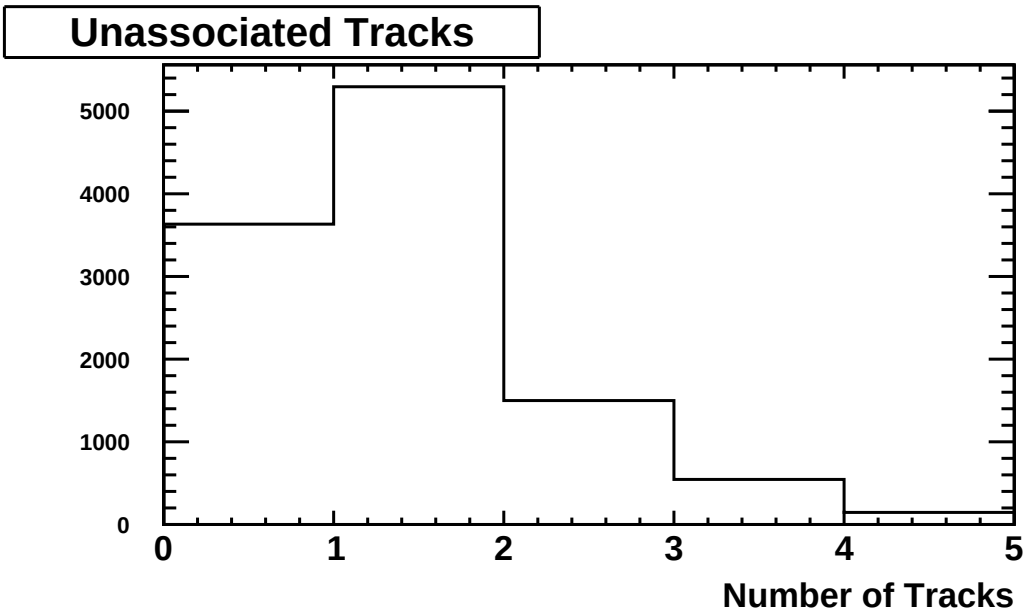

Figure 14.6: Multiplicity of unassociated tracks in the jets with one secondary vertices for the same sample of $Z \to b\bar{b}$ events as Figure 14.1.

the closest approach of the track to the vertex line must be less than 0.5 radians.

- The displacement vector from the primary vertex to the vertex point, which is defined as the point on the track that is closest to the vertex line, and the direction of the track must be able to be put in the same hemisphere.
- The distance between the primary vertex and vertex point must be within the range $0.3 - 30$ mm.
- The distance between the primary vertex and the vertex point must be more than 10 times greater than the distance between the vertex point and the vertex line.

The tracks passing these constraints were classified and stored as pseudo-vertices. The number of pseudo-vertices found in the jets from $Z \to b\bar{b}$ events, with one secondary vertex are shown in Figure 14.7. To test if a track passes the criteria to be a pseudo-vertex, its vertex point has to be found. This is described in the following section.

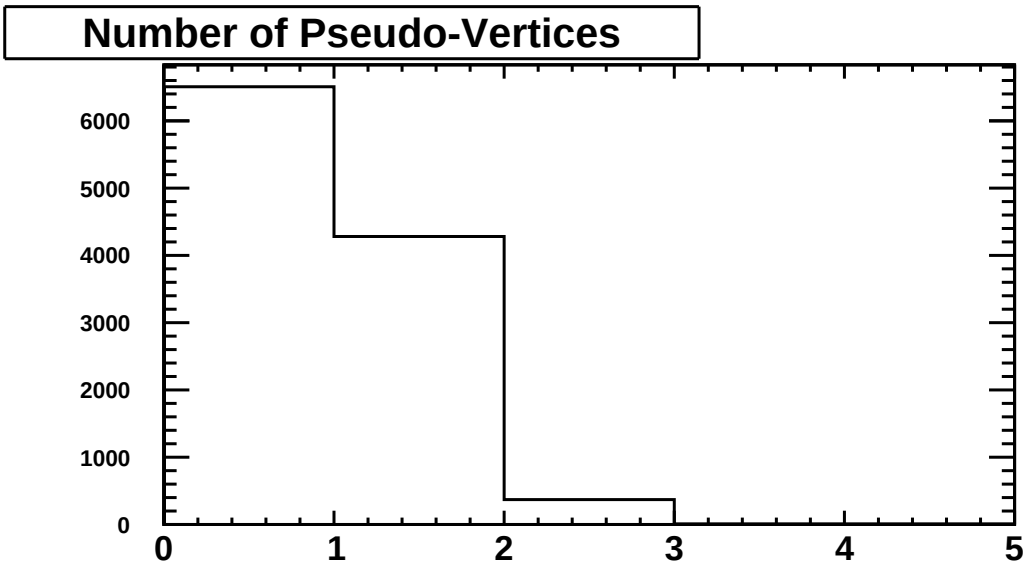

Figure 14.7: Number of pseudo-vertices found in the jets with one secondary vertex for the same sample of $Z \to b\bar{b}$ events as Figure 14.1.

14.1.5 Vertex Point

The vertex point is the point on the particle track which is closest to the line connecting the primary and the secondary vertex, referred to as vertex line; this is illustrated in Figure 14.8. Since, the coordinates and the momentum at the production point of a particle track are known, these can be used to calculate the coordinates and the momentum at the vertex point.

Equation 6.3, defining the position coordinates and the momentum components of the track at any arbitrary point, are functions of the arc length, $s_\perp$, of the particle track. Coordinates and the momentum of the particle at different points on the track can be obtained by varying $s_\perp$ in this system of equations.

To find the vertex point in the study reported in the previous section, the track was traversed with a step of 1 μm, in both directions from the production vertex of the particle until the distance of the point on the track from the origin exceeded 30 mm. The distance from the vertex line was calculated at each step. The point, for which this distance was minimum, was chosen as the vertex point. The momentum at the vertex point was calculated using Equation 6.3.

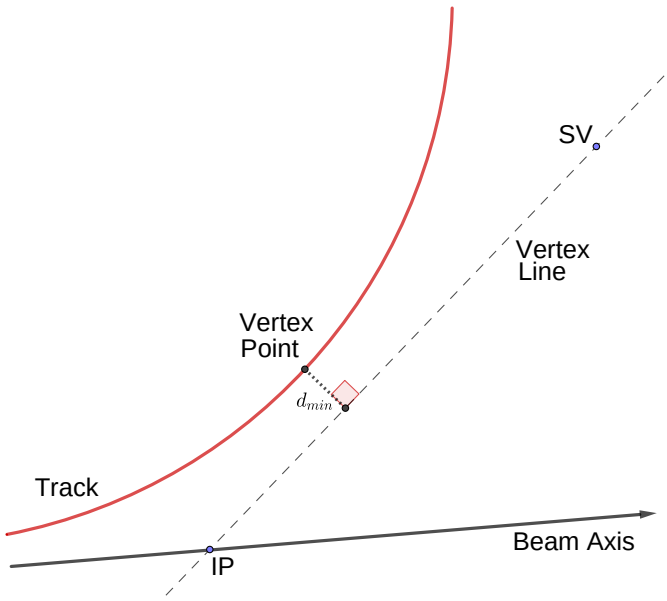

Figure 14.8: Vertex point and vertex line. The red curve represents the track, IP stands for interaction point and SV stands for secondary vertex. d_{min} is the minimum distance from the track to the vertex line

The distance between the vertex point and the primary vertex, the opening angle between the vertex line and the particle momentum at the vertex point, and the position of the vertex point with respect to the primary vertex were used to check whether a track is a pseudo-vertex.

14.2 Performance Review

After implementing the steps presented in Section 14.1, each event would have a primary vertex, $0-2$ secondary vertices per jet, and 0 or more pseudo-vertices per jet. Therefore, all jets can be classified in four categories shown in Table 14.1.

	Secondary Vertices	Pseudo-vertices
1)	0	-
2)	1	0
3)	1	>0
4)	2	-

Table 14.1: Categories to classify different flavours of the hadronic jets from decay events.

Each of these categories are enriched in events with the Z boson decaying to a certain flavour of quark-antiquark pair. The majority of $Z \to q'\bar{q}'$ events, with $q' \equiv (u, d, s)$, are in category $1)$; $Z \to c\bar{c}$ events from category $2)$ are the most likely to be accurately identified; and events from categories $3)$ and $4)$ are mostly $Z \to b\bar{b}$ events with a very little contamination from other flavoured decay events.

A set of $Z \to q\bar{q}$ events were classified in this way; $10{,}000$ events with $q \equiv b$, $q \equiv c$, and $q \equiv (u, d, s)$ each. The distribution of the jets from these events in the four categories introduced above is shown in Table 14.2.

(#vtx,#pseudo-vtx)	bottom jets	charm jets	light jets
$(0, -)$	17.9%	60.1%	97.5%
$(1, 0)$	34.8%	37.7%	2.4%
$(1, > 0)$	23.1%	1.4%	0%
$(2, -)$	24.3%	0.4%	0.1%

Table 14.2: The distribution of jets from $Z \to q\bar{q}$ events, with $q \equiv b, c, (u, d, s)$, categorised by the numbers of reconstructed secondary vertices and pseudo-vertices.

14.3 Algorithm

This section summarises the algorithm that introduces a multi-step technique for classifying the hadronic decay events relying on reconstructing and refining the secondary vertices and it is inspired from the methods presented in the LCFIPlus framework[29][32].

Before fitting the particle tracks to find the primary and the secondary vertices, all the tracks are clustered into jets.

14.3.1 Primary Vertex Finding

Particle tracks from all jets participate in this step. All of the tracks from the event are classified into two categories; primary tracks and non-primary tracks using the transverse impact parameter significance.

The tracks that have a transverse impact parameter significance within a threshold range are classified as primary tracks and the remaining tracks are classified as non-primary tracks. The performance of the algorithm is sensitive to this threshold range, which can be chosen by looking at the distribution of the transverse impact parameter significance for all tracks.

The primary tracks are fitted to a vertex to get the position of the primary vertex and the associated χ^2 value.

All further steps are executed for each jet individually.

14.3.2 Secondary Vertex Finding

V^0 rejection with the set of 'tight' constraints, as described in Chapter 11, is performed on the set of non-primary tracks. The pairs of tracks that are identified as forming a V^0 vertex, consistent with these constraints, are removed from the vertex finding procedure.

To find a seed vertex among the non-primary tracks, all possible track pairs are fitted to find a common vertex for each track pair. These two-track vertices are subjected to the constraints presented in Section 14.1.3.

Upon finding the best two-track vertex, additional tracks are attempted to be attached to this seed vertex to create a vertex with a higher track multiplicity. A track is added to the seed vertex if the χ^2 contribution of the track in the resulting vertex is smaller than a threshold value and the vertex satisfies the constraints presented in Section 14.1.3, with the exception of V^0 selection. Out of all the tracks which pass these selection constraints, the track, which results in a lowest vertex χ^2 value is chosen and added to the seed vertex.

This process is reiterated until no more tracks can be combined to the vertex following the stated criteria. Once a secondary vertex is found, the tracks forming this vertex are removed and the entire procedure is then repeated to find further secondary vertices from the remaining tracks. Secondary vertices are reconstructed until no seed vertices can be found.

14.3.3 Jet Vertex Refining

The two steps followed during vertex refining are vertex combining and finding single-track vertices.

Vertex combining is performed for the jets with three or more reconstructed secondary vertices. It proceeds via the steps presented in Section 14.1.4. After this procedure has been performed, all the jets have at most two secondary vertices.

The next step is performed to find single-track vertices or pseudo-vertices. For a track to be classified as a pseudo-vertex, it needs to satisfy the criteria mentioned in Section 14.1.4.

After the vertex refining procedures, all jets would fall in one of the four following categories. They would either have 0 secondary vertices, 1 secondary vertex and 0 pseudo-vertices, 1 secondary vertex and 1 or more pseudo-vertices, or 2 secondary vertices. This has been summarised in Table 14.1. These categories are enriched in the jets from the decay events to a certain flavour of quark-antiquark pair.

15 Perspectives

Accurately identifying the flavour of the hadronic decay channels of the Higgs boson is essential for high-precision measurements of its properties. The algorithms presented here have been studied only for two-jet events. However, at future e^+e^- colliders like FCC-ee, the Higgs boson will be dominantly produced via the Higgs-strahlung process and a majority of hadronic decay events will be four-jet events. This will certainly increase the chances of misidentification, if only slightly. Therefore, the algorithms need to be studied and optimised for such events.

In the Impact Parameter Algorithm, demonstrated in Section 12.2, the transverse impact parameter significance can be used to obtain the tagging parameter instead of the absolute value of the transverse impact parameter. To further reduce the contamination of light quarks, V^0 rejection can be performed on the set of particle tracks before putting a threshold on the magnitude of impact parameter. This will also make the algorithm less sensitive to this threshold. Although, the V^0 rejection will have to be performed on the entire set of tracks as the separation of primary and non-primary tracks is not performed in this algorithm. However, it is not advisable to use this algorithm for identifying the decay events to charm or light quarks.

There is also scope to further improve the flavour tagging efficiency of the algorithm studied in Section 14.1. The order of the two steps of vertex finding and jet clustering can be reversed along with implementing a modified clustering algorithm, this may result in improved classification of the jets in the four categories for event with more than two jets. The vertex refining step

also has some scope for optimisation, as has also been suggested in Section 14.1.4.

The study presented in Chapter 14 classifies the jets from the decay events into four categories, but further analysis is required to identify the hadronic flavour of these events. To do this, a set of variables can be defined for the categories defined in Table 14.1 that can be used as inputs in a mutivariate classifier. Such variables include, the transverse and longitudinal impact parameter significance and momentum of the track with the highest transverse impact parameter significance, number of identified electrons and muons, decay lengths of the vertices in the jet, the invariant masses of the secondary vertices etc. Some of these variables depend on the energy of the jets and they can be normalised accordingly. These can be analysed using a multivariate classifier. LCFIPlus framework[29] report the results of such an analysis. Since the study has been conducted for two-jet events, the performance of the two different orderings of vertex finding and jet clustering steps is very similar, but for multi-jet events, performing jet clustering after vertex finding using a modified clustering algorithm has significant advantages. In such a jet clustering algorithm, the soft lepton taggers can also be used to improve the accuracy of the clustering.

16 Bibliography

[1] P.A. Zyla et al. (Particle Data Group). *Review of Particle Physics*. 2020. URL: http://pdg.lbl.gov/2020/html/authors_2020.html.

[2] Mark Thomson. „Modern Particle Physics“. In: 2013.

[3] A Lopez-Fernandez, J.C Ramão, F de Campos, *et al.* „Model-independent Higgs boson mass limits at LEP“. In: *Physics Letters B* 312.1-2 (Aug. 1993), pp. 240–246. ISSN: 0370-2693. DOI: 10.1016/0370-2693(93)90518-m. URL: http://dx.doi.org/10.1016/0370-2693(93)90518-M.

[4] G. Dissertori. „"The pre-LHC Higgs hunt"“. In: *Philosophical Transactions of the Royal Society A* 373 (Jan. 2015). ISSN: 1471-2962. DOI: 10.1098/rsta.2014.0039. URL: https://royalsocietypublishing.org/doi/10.1098/rsta.2014.0039.

[5] "ATLAS Collaboration". „Observation of a new particle in the search for the Standard Model Higgs boson with the ATLAS detector at the LHC“. In: *Physics Letters B* 716.1 (Sept. 2012), pp. 1–29. ISSN: 370-2693. DOI: 10.1016/j.physletb.2012.08.020. URL: http://www.sciencedirect.com/science/article/pii/S037026931200857X.

[6] CMS Collaboration. „Observation of a new boson at a mass of 125 GeV with the CMS experiment at the LHC“. In: *Physics Letters B* 716 (Sept. 2012), pp. 30–61. ISSN: 370-2693. DOI: 10.1016/j.physletb.2012.08.021. URL: http://www.sciencedirect.com/science/article/pii/S0370269312008581.

[7] Howard Georgi and Sheldon L. Glashow. „Gauge Theories Without Anomalies“. In: *Phys. Rev. D* 6 (2 July 1972), pp. 429–431. DOI: 10.1103/PhysRevD.6.429. URL: https://link.aps.org/doi/10.1103/PhysRevD.6.429.

[8] Lyndon Evans. „The Large Hadron Collider“. In: *Annual Review of Nuclear and Particle Science* 61.1 (2011), pp. 435–466. DOI: 10.1146/annurev-nucl-102010-130438. eprint: https://doi.org/10.1146/annurev-nucl-102010-130438. URL: https://doi.org/10.1146/annurev-nucl-102010-130438.

[9] R. Assmann, M. Lamont, and S. Myers. „A brief history of the LEP collider“. In: *Nucl. Phys. B Proc. Suppl.* 109B (2002). Ed. by F.L. Navarria, M. Paganoni, and P.G. Pelfer, pp. 17–31. DOI: 10.1016/S0920-5632(02)90005-8.

[10] Nan Phinney. *SLC Final Performance and Lessons*. 2000. arXiv: physics/0010008 [physics.acc-ph].

[11] FCC Collaboration, A. Abada, M. Abbrescia, *et al.* „FCC-ee: The Lepton Collider: Future Circular Collider Conceptual Design Report Volume 2“. English (US). In: *European Physical Journal: Special Topics* 228.2 (June 2019), pp. 261–623. ISSN: 1951-6355. DOI: 10.1140/epjst/e2019-900045-4.

[12] The CEPC Study Group. *CEPC Conceptual Design Report: Volume 1 - Accelerator*. 2018. arXiv: 1809.00285 [physics.acc-ph].

[13] Keisuke Fujii, Christophe Grojean, Michael E. Peskin, *et al. Physics Case for the 250 GeV Stage of the International Linear Collider*. 2017. arXiv: 1710.07621 [hep-ex].

[14] M.J. Boland et al. CLIC Collaboration. *Updated baseline for a staged Compact Linear Collider*. 2016. DOI: 10.5170/CERN-2016-004.

[15] „The International Linear Collider Technical Design Report - Volume 3.II: Accelerator Baseline Design“. In: (2013). Ed. by Chris Adolphsen *et al.* arXiv: 1306.6328 [physics.acc-ph].

[16] Lucie Linssen, Akiya Miyamoto, Marcel Stanitzki, *et al. Physics and Detectors at CLIC: CLIC Conceptual Design Report*. 2012. arXiv: 1202.5940 [physics.ins-det].

[17] M. Bicer, H. Duran Yildiz, I. Yildiz, *et al.* „First look at the physics case of TLEP“. In: *Journal of High Energy Physics* 2014.1 (Jan. 2014). ISSN: 1029-8479. DOI: 10.1007/jhep01(2014)164. URL: http://dx.doi.org/10.1007/JHEP01(2014)164.

[18] Halina Abramowicz, Roger Forty, and the Conveners. *Physics Briefing Book*. Oct. 2019. URL: https://cds.cern.ch/record/2691414/files/Briefing_Book_Final.pdf.

[19] W Kilian, M Krämer, and P.M Zerwas. „Higgs-strahlung and WW fusion in e+e collisions“. In: *Physics Letters B* 373.1-3 (Apr. 1996), pp. 135–140. ISSN: 0370-2693. DOI: 10.1016/0370-2693(96)00100-1. URL: http://dx.doi.org/10.1016/0370-2693(96)00100-1.

[20] Patrizia Azzi, Colin Bernet, Cristina Botta, *et al. Prospective Studies for LEP3 with the CMS Detector*. 2012. arXiv: 1208.1662 [hep-ex].

[21] Fenfen An, Yu Bai, Chunhui Chen, *et al.* „Precision Higgs physics at the CEPC“. In: *Chinese Physics C* 43.4 (Apr. 2019), p. 043002. ISSN: 2058-6132. DOI: 10.1088/1674-1137/43/4/043002. URL: http://dx.doi.org/10.1088/1674-1137/43/4/043002.

[22] N. Bacchetta, J. -J. Blaising, E. Brondolin, *et al. CLD – A Detector Concept for the FCC-ee*. 2019. arXiv: 1911.12230 [physics.ins-det].

[23] Dominik Arominski *et al.* „A detector for CLIC: main parameters and performance“. In: (Dec. 2018). arXiv: 1812.07337 [physics.ins-det].

[24] Paul Avery. *Applied Fitting Theory IV: Formulas for Track Fitting*. 1992. URL: https://www.phys.ufl.edu/~avery/fitting/fitting4.pdf.

[25] Franco Bedeschi. *Franco Bedeschi: RD$_F$A : $Software$*. 2019. URL: https://www.pi.infn.it/~bedeschi/RD_FA/Software/.

[26] Torbjörn Sjöstrand, Stephen Mrenna, and Peter Skands. „A brief introduction to PYTHIA 8.1“. In: *Computer Physics Communications* 178.11 (June 2008), pp. 852–867. ISSN: 0010-4655. DOI: 10.1016/j.cpc.2008.01.036. URL: http://dx.doi.org/10.1016/j.cpc.2008.01.036.

[27] Torbjörn Sjöstrand, Stephen Mrenna, and Peter Skands. „PYTHIA 6.4 physics and manual“. In: *Journal of High Energy Physics* 2006.05 (May 2006), pp. 026–026. ISSN: 1029-8479. DOI: 10.1088/1126-6708/2006/05/026. URL: http://dx.doi.org/10.1088/1126-6708/2006/05/026.

[28] Matteo Cacciari, Gavin P. Salam, and Gregory Soyez. „FastJet user manual“. In: *The European Physical Journal C* 72.3 (Mar. 2012). ISSN: 1434-6052. DOI: 10.1140/epjc/s10052-012-1896-2. URL: http://dx.doi.org/10.1140/epjc/s10052-012-1896-2.

[29] Taikan Suehara and Tomohiko Tanabe. „LCFIPlus: A framework for jet analysis in linear collider studies“. In: *Nuclear Instruments and Methods in Physics Research Section A: Accelerators, Spectrometers, Detectors and Associated Equipment* 808 (Feb. 2016), pp. 109–116. ISSN: 0168-9002. DOI: 10.1016/j.nima.2015.11.054. URL: http://dx.doi.org/10.1016/j.nima.2015.11.054.

[30] T. V. Obikhod and I. A. Petrenko. *B-tagging and searches for new physics beyond the Standard Model*. 2019. arXiv: 1901.07885 [hep-ph].

[31] Taikan Suehara, Tomohiko Tanabe, and Satoru Yamashita. *Improved jet clustering algorithm with vertex information for multi-bottom final states*. 2011. arXiv: 1110.5785 [hep-ex].

[32] D. Bailey, E. Devetak, M. Grimes, *et al.* „The LCFIVertex package: Vertexing, flavour tagging and vertex charge reconstruction with an ILC vertex detector“. In: *Nuclear Instruments and Methods in Physics Research Section A: Accelerators, Spectrometers, Detectors and Associated Equipment* 610.2 (Nov. 2009), pp. 573–589. ISSN: 0168-9002. DOI: 10.1016/j.nima.2009.08.059. URL: http://dx.doi.org/10.1016/j.nima.2009.08.059.